Aerodynamic installation effects for tip-mounted tractor propeller and nacelle

O.M. Lubbers

TU Delft

Aerodynamic installation effects for tip-mounted tractor propeller and nacelle

by

O.M. Lubbers

Composition of the thesis committee:	
Chair:	dr. M. F. M. Hoogreef
Examiner:	dr. L. Lima Pereira
Supervisor:	dr. T. Sinnige
Assistant supervisor:	J. Goyal
Project Duration:	February, 2023 - June, 2024
Faculty:	Faculty of Aerospace Engineering, Delft

TU Delft

Preface

This thesis marks the end of my time as a student at Aerospace Engineering at Delft University of Technology. For this, I would like to express my gratitude for every person that have made this education and all other learning opportunities around the faculty possible.

First of all, my supervisors who have guided me for the past years. Dr. Tomas Sinnige and almost-dr. Jatinder Goyal, thank you for your guidance, support and knowledge along the way. The best of luck to you and may our paths cross again some time in this endeavour towards sustainable aviation.

Additionally, I would like to thank dr. M. F. M. Hoogreef and dr. L. Lima Pereira for being on my defense committee.

Last but not least, I would not be who I am without my social support. Thank you, friends and family, for your patience and unconditional support. You inspire me to keep learning and to follow my heart.

O.M. Lubbers
Delft, June 2024

Summary

Aerodynamics of wingtip-mounted tractor propellers is investigated using Computational Fluid Dynamics (CFD) simulations. As part of FutPrint50 research, the nacelle can be removed in experimental research when the propeller location is investigated. The objective of this thesis is to numerically quantify the effect of excluding the nacelle in tip-mounted propeller research on aerodynamic performance.

This is done by modelling four configurations in a representative geometry. With these configurations, the effect of adding or removing the nacelle can be compared, with and without the propeller installed. The geometry used is taken from the experimental research as much as possible, as well as the operating conditions. Reynolds Averaged Navier Stokes (RANS) equations are used, as it is concluded from literature that this performs well.

For the propeller modelling, an actuator disk model is used because it saves computational cost. Before the nacelle effect is investigated with the propeller installed, the propeller loading is chosen. It is desired to use an isolated loading case, since this is more versatile. For the loading cases, the trends observed is the same, and the differences can be explained by the change in input load. Therefore, the isolated propeller loading is used for further research.

Then, dependency studies are done to verify the set-up settings. A domain dependency study to define the length of the wind tunnel, and a grid dependency study, checking the fineness of the grid and estimating the error for the chosen grid. From the domain dependency study it was concluded that an inlet length of 15 MAC (7.2m) can be used, with an outlet length of 20 MAC (9.6m). From the grid dependency study, the most accurate grid that still has an acceptable computational cost is chosen. With five grids used, the output parameters seem oscillatory, so the discretization uncertainty is calculated with a higher uncertainty. The lift coefficient uncertainty is 1.32 % for the chosen grid, and the drag coefficient uncertainty is 0.3-9.5%. These dependency studies test and verify the model for upcoming results.

The first results are without the propeller installed yet. It is observed that the overall lift of the wing increases, as well as the span distribution. Excluding the nacelle and wing tip, the drag change is very small and thus the lift over drag increases by 2.8%. When the nacelle and wingtip is included, this results in a drag increase as well and the lift over drag of the wing decreases by 7.4%.

Also with the propeller installed, these effects are visible. The lift and the drag increase when the nacelle is added, overall decreasing the lift over drag. Furthermore, by investigating the swirl angle, the behaviour of the vortices as an installation effect of the nacelle is analysed. The swirl in the wake moves outboard when the nacelle is added, and the maximum value increases. This is due to the nacelle being located more outboard than the wing tip, and a higher pressure differential between the pressure and suction side of the wing.

Lastly, the effect of installing the propeller is compared with and without the nacelle present. For both the performance parameters as well as the wake swirl, the results without the nacelle are conservative compared to the results with nacelle, whilst showing the same trend. As expected, adding the propeller attenuates the swirl angle overall in both cases, and both lift and drag are increased. Since this effect is bigger with the nacelle installed, without the nacelle will thus underestimate the effect but still show it.

Overall, these findings underscore the importance of considering the installation effects of tip-mounted nacelles on wing aerodynamics, with implications for wing performance and wake characteristics. When research is done on the spanwise or vertical position of the propeller, the effect of the nacelle needs to be accounted for because of the magnitude and the location of the flow properties.

The nacelle has a significant effect on the performance of the wing, and the flow field characteristics. The lift is increased across the wing, the nacelle itself adds drag, the vortex shifts, and the total pressure

in the wake changes. It is good to be aware of the changes as described above that the nacelle will entail. However, when investigating the effect of tip-mounted propellers, the same result trends are found though without the nacelle the values at most are conservative. Therefore, with the implications of this decision in mind, it can be argued that moving the nacelle upstream is a justifiable assumption.

Contents

Nomenclature

Abbreviations

Abbreviation	Definition
AD	Actuator Disk
AR	Aspect Ratio
BOI	Body Of Influence
CFD	Computational Fluid Dynamics
CFL	Courant–Friedrichs–Lewy
DNW	German-Dutch Wind Tunnels
FutPrint50	Future Propulsion and Integration 2050
ICAO	International Civil Aviation Organisation
LST	Low-Speed Tunnel
MAC	Mean Aerodynamic Chord
PIV	Particle Image Velocimetry
RANS	Reynolds-Averaged Navier-Stokes
UDF	User Defined Function

Symbols

Symbol	Definition	Unit
$\overline{c}$	Mean chord length	[m]
cd_l	Local drag coefficient, $2D/\rho V^2 c_{local}$	[-]
cd_t	Integrated drag coefficient, $\int_0^s (2D/\rho V^2 S) ds$	[-]
C_f	Skin friction coefficient	[-]
cl_l	Local lift coefficient, $2L/\rho V^2 c_{local}$	[-]
cl_t	Integrated lift coefficient, $\int_0^s (2L/\rho V^2 S) ds$	[-]
D	Propeller diameter	[m]
J	Advance ratio, V_∞ / n D	[-]
k	Specific heat ratio	[-]
M	Mach number	[-]
n	Rotational speed	[rad/s]
p_0	Total pressure	[Pa]
p_{stat}	Static pressure	[Pa]
P	Sectional power	[Wm^{-1}]
P'_c	Sectional power coefficient, P / ($\rho V^3 D$)	[-]
Q	Sectional torque, $P/2\pi n$	[Wm^{-1}]
Re	Reynolds number	[-]
S	Wing planform surface area	[m^2]
s	Span	[m]
T	Sectional thrust	[Nm^{-1}]
T'_c	Sectional thrust coefficient, T / ($\rho V^2 D$)	[-]
U	Discretization Uncertainty	[%]
V	Velocity	[ms^{-1}]
V_∞	Freestream velocity	[ms^{-1}]
$\frac{\nu_t}{\nu}$	Turbulent viscosity ratio	[-]
V_τ	Frictional velocity	[ms^{-1}]

Symbol	Definition	Unit
γ	Nacelle tilt angle	[degrees]
μ	Dynamic viscosity	[kg m^{-1} s^{-1}]
Ω	Rotational velocity	[rad s^{-1}]
ρ	Density	[kg m^{-3}]
τ_w	Wall shear stress, $0.5C_f\rho V^2$	[Pa]

1

Introduction

The aviation industry is looking for ways to decarbonise. The International Civil Aviation Organisation (ICAO) has the aspirational goal of net-zero carbon emissions by 2050, which has to be done partially by improving fuel efficiency and technology [1]. There is no silver bullet to make the aviation industry more sustainable [2], so industry and academia are looking for different solutions. One potential part of the solution would be to fly more with electric aircraft. Electric flight would be a solution for the slower flying, short range aircraft [2]. As electric motors are generally lighter, this enables distributed propulsion and wingtip-mounted propellers [3]. This is already illustrated with experimental aircraft such as NASA's X-57 Maxwell [4] and GL-10 [5]. Also, the original design of the Eviation Alice had wing-tip mounted propellers as well [6]. This recently increasing interest in wingtip-mounted propellers is due to the potential benefits of increased lift, lower induced drag, and overall improved fuel efficiency. Meanwhile, the aerodynamic interaction effects between the wing and the propeller slipstream are complex and not fully understood yet.

FutPrInt50 is an European research initiative aimed at developing new technologies and strategies for reducing the environmental impact of aviation. The name FutPrInt is an acronym for FUTure PROpulsion and INTegration [7]. This research is done as part of this project, working towards a 50-seat hybrid-electric regional aircraft. The goal of the FutPrInt50 project is to provide the aviation industry with the knowledge and tools needed to develop more sustainable and efficient aircraft designs, and to help mitigate the environmental impacts of air travel. The research in this thesis adds to the field by doing Computational Fluid Dynamics (CFD) analysis on the propeller integration.

Research into tip-mounted propellers has traditionally been conducted using wind tunnels, such as the low-speed tunnel (LST) of the German-Dutch Wind Tunnels (DNW) used in the FutPrInt research. In these studies, a scale model is used to simulate aerodynamic behavior. However, the shape and location of the nacelle, which houses the propulsion system, is not always representative of the case being analyzed. This makes it challenging to validate whether removing the nacelle or altering its shape is valid.

Furthermore, the choice is sometimes made to isolate the nacelle upstream, as shown in Figure 1.1a. For instance, recent research in Braunschweig aimed to adjust the propeller's position relative to the wing, as depicted in Figure 1.1b. While these wind tunnel experiments serve as validation of disk models, they neglect the presence of a nacelle attached to the wing [8]. This effect can be tested with Computational Fluid Dynamics (CFD) models, which can investigate how removing the propeller installation would affect the results.

In this research, CFD simulations will be performed using a 3D model that matches the geometry of the models used in the wind tunnel testing. This approach is chosen for several reasons. Wind tunnels are expensive and often fully booked far in advance. If computer simulations can contribute to the research, this could potentially save resources otherwise spent on experimental setup. Moreover, numerical modeling offers benefits that experimental research does not. The main advantage of using numerical modeling for this thesis is the flexibility it provides in relocating the propeller to any spatial coordinate without restrictions. The propeller in this thesis will be modeled by replacing the propeller with

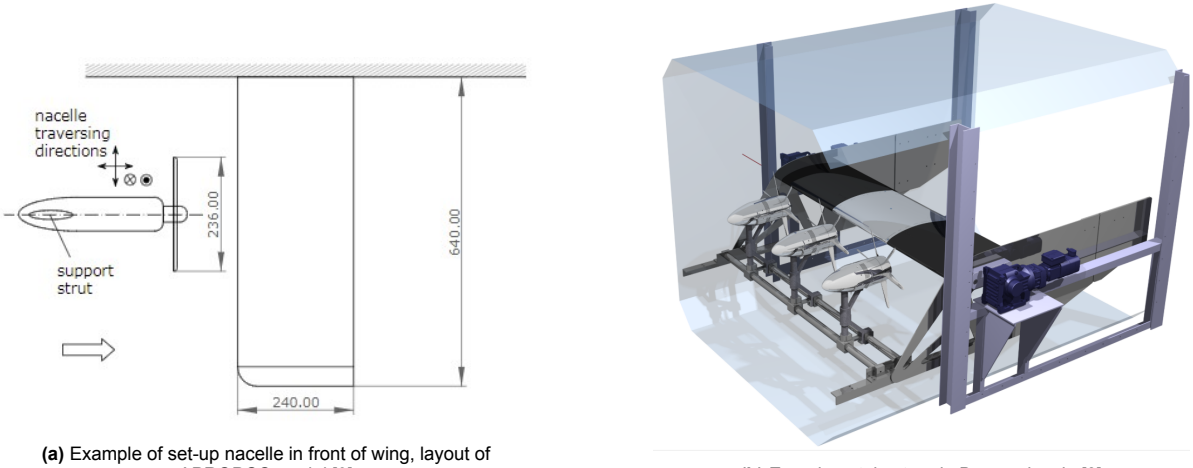

(a) Example of set-up nacelle in front of wing, layout of APROPOS model [9]

(b) Experimental set-up in Braunschweig [8]

Figure 1.1: Experimental research set-up examples with isolated propeller in front of the wing.

distributions of momentum and energy sources representing the disk, a method known as the actuator disk (AD) model. By utilizing the actuator disk model in our CFD simulations, the numerical set-up of this research adds to the experimental modelling methods in wind tunnels.

The objective of this thesis is to numerically quantify the effect of excluding the nacelle in tip-mounted propeller research on aerodynamic performance. To achieve this, an inboard-up rotating propeller will be used in the context of the FutPrInt50 research. The results will be used to investigate the swirl angle and wingtip vortex, as well as the performance of the wing. The extent of this research can be summarised in three research questions.

- How does the nacelle on the tip influence the performance parameters of the wing?
- What are the other installation effects of the tip-mounted propeller and nacelle?
- To what extent can tip-mounted propellers be modelled by a disk model without a nacelle?
- How are the results of adding a propeller influenced by the presence of a nacelle?

Firstly, the aerodynamic performance parameters of the wing are analyzed, including wing loading and various lift and drag components. These values are compared to understand the impact of the nacelle and propeller. This is crucial as the goal of tip-mounted propellers is to enhance overall efficiency, making these performance parameters key results of the research. Next, the flow field is examined for other effects, such as changes in shear or local flow on the wing, and the magnitude and location of vortices. The effects of both having the propeller on or off and installing the nacelle or not are analyzed, to better understand the flow phenomena of tip-mounted propellers. Finally, the actuator disk method chosen for this study is analyzed. While it is beyond the scope to compare this method with a full propeller model, the strengths and limitations of the disk model on the nacelle's influence can still be identified. Furthermore, the impact of the choice of input loading distributions are investigated, summarised in the sub-question: "to what extent can isolated propeller loading be used in a disk model for tractor tip-mounted propellers?". These questions together allow for an investigation of the effect of the nacelle's presence and a determination of whether it can be removed in experimental research.

The research context and the selection process for the numerical method are given in chapter 2. Details regarding the numerical method set-up and the exclusion of the nacelle can be found in chapter 3. In this chapter, the verification process through dependency studies is discussed, specifically in section 3.3. The aerodynamic performance and other results are discussed in chapter 4. After which the conclusions are written in chapter 5, and recommendations are made in chapter 6.

2

Literature review

Before the set-up and methodology are discussed, the relevant aerodynamic phenomena and the background on numerical modelling are discussed in this chapter. The aerodynamic phenomena are limited to the most important ones that will be relevant later in the results in chapter 4 as well, and for the modelling the reasoning for the chosen numerical method is given while the design decisions within this method are discussed in the set-up in chapter 3.

2.1. Aerodynamic effect of tractor propeller on the wing

First, the aerodynamic phenomena around wingtip-mounted tractor propellers are investigated. The slipstream of a thrust-generating propeller is discussed, as well as more specifically research done on tip-mounted propellers. Furthermore, the vertical position and research done on this is discussed, because this is relevant for the aim of this thesis. And finally, the interaction effect of propeller-wing system with a tractor propeller, which will set the basis for the analysis of the results later in this thesis.

2.1.1. Propeller slipstream

Since this thesis looks into the aerodynamic interaction effects of wingtip-mounted propellers, first this section will explore what elements are interacting. One of these elements is the propeller slipstream, that will interact with the wing and the wing tip vortex downstream. The propeller slipstream is defined in order to see what parameters will be looked at.

The propeller slipstream is the flow of air that is disrupted by the movement of a propeller, behind the propeller. The velocity behind the propeller in flight direction is higher than the freestream velocity, because thrust is generated by adding momentum to the flow. Also there is a rotational velocity present. Each propeller blade is like a wing, but in this function the resulting forces are thrust and torque. Also, each propeller blade creates downwash, which can be split up into two components. The velocity of the deflected flow in flight direction is induced thrust, and the rotational motion perpendicular to the thrust is called swirl. Swirl is an energy loss and should be minimized.

Another effect of the slipstream, also without taking into account the rotational component of the flow, is the slipstream contraction. Due to the increased flow velocity, the average dynamic pressure in the slipstream increases, and by the conservation of mass the slipstream thus contracts, as shown in Figure 2.1. The wing is placed within this effect, as it is a tractor propeller. This results in the wing having a positive angle of attack when placed below the propeller axis, as seen in 'position 1' in Figure 2.1. And when moved up above the propeller axis, the wing experiences a negative angle of attack, as seen in 'position 2'. This will result in local lift and drag changes on the wing.

The vortex system in the propeller slipstream consists of all sources that create vortices. The tip of each propeller blade, the root of each propeller blade, and a sheet of trailing vortices of each blade [11]. An example of an illustrated propeller slipstream with CFD is shown in Figure 2.2b. Two stream elements can be clearly seen in this image: blade wakes and the nacelle vortex. The nacelle vortex is

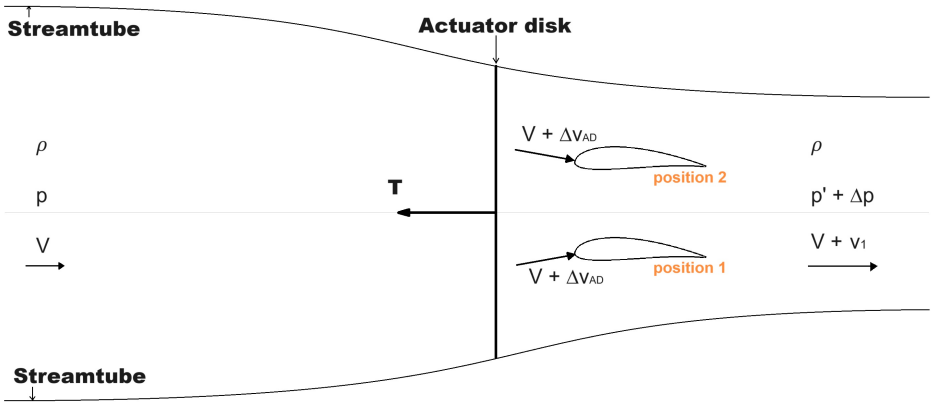

Figure 2.1: Slipstream through an actuator disk with positive thrust, based on [10].

not part of this propeller slipstream, but generated by the junction of the nacelle with the wing leading edge. Note here that in this picture, the wing is at high angle of attack and this is the suction side of the wing. The blade wakes most prominently shown are due to the propeller tip vortices, creating these vortical structures.

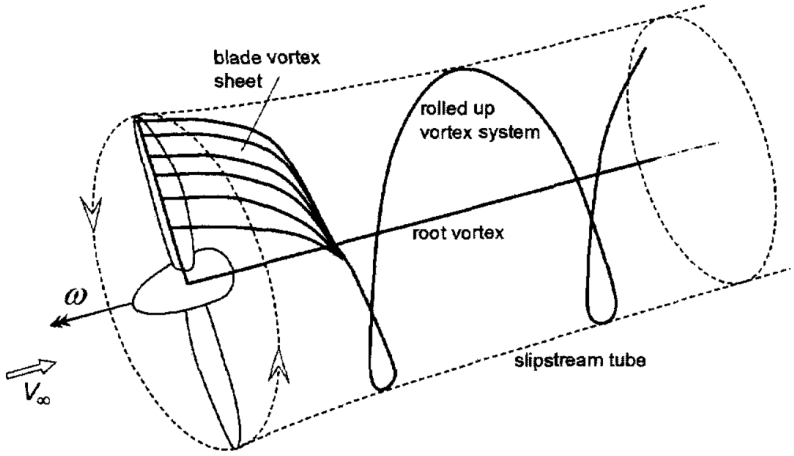

(a) Helical vortex system and slipstream tube created by propeller [12].

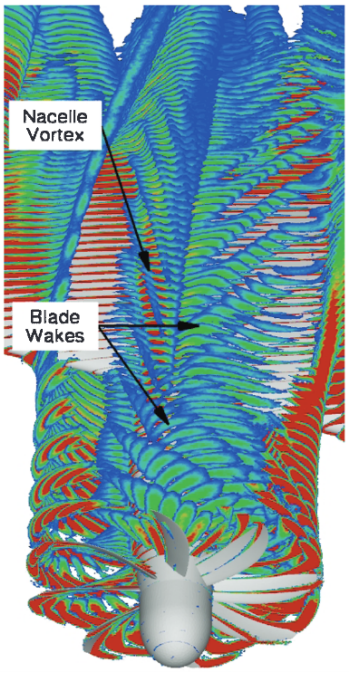

(b) Flow topology produced with CFD by [13].

Figure 2.2: Propeller slipstream visualised.

So when looking at the propeller slipstream in the system of this thesis, the flow features above are to be recognized. Although the propeller will be modelled with an actuator disk for this research, the slipstream and the swirl angle will be seen.

2.1.2. Tractor propeller system

The integration effect of having a tractor propeller, tip-mounted or not, is investigated and used in this research. With this theory, the results are analysed later. The presence of the wing has an effect on the propeller loading, and the presence of the propeller has an effect on the wing behind it. In this

section, the effects of the tractor propeller on the wing are discussed. Because a disk model will be used, the effect of the wing on the propeller is discussed in the set-up in subsection 3.2.2. The tractor propeller has two main effects on the wing itself: it alters the lift distribution, and it leads to swirl recovery.

The lift distribution is altered due to the upwash behind the up-going blade and the downwash behind the down-going blade. At the upwash side, the angle of attack at the wing increases and at the downwash side the angle of attack decreases. On both sides, the dynamic pressure increases [14]. The increase of angle of attack at the upwash side has a beneficial effect on the lift and drag while the downwash side has a negative effect [9]. Figure 2.3a shows this effect of the inboard up propeller in the solid line on both sides of the propeller. Placing the propeller physically at the wing tip, the negative effects such as in section W-III might be mitigated by the absence of a wing at the downwash side.

The velocities generated by a propeller can be decomposed in an out-of-plane velocity that generates thrust, and a rotational velocity that is called the swirl. The propeller slipstream swirl is a loss of energy, as it does not generate thrust. However, due to this angular velocity, there is an induced upwash and downwash at the wing. Next to the changing lift distribution, the changing resultant force due to the downwash and upwash also has a component in the drag direction. Generally, this resultant force on both sides together will create negative drag, which essentially is an additional thrust component. This is why the axial component of this resultant force is referred to as swirl recovery. This effect for both sides of the propeller is illustrated in Figure 2.3b, where the cambered airfoil is relevant for this thesis. Again, for wingtip-mounted propellers, the down going blade side does not have this direct effect on the wing because there is no wing behind it, and it can be observed that the positive effect increases.

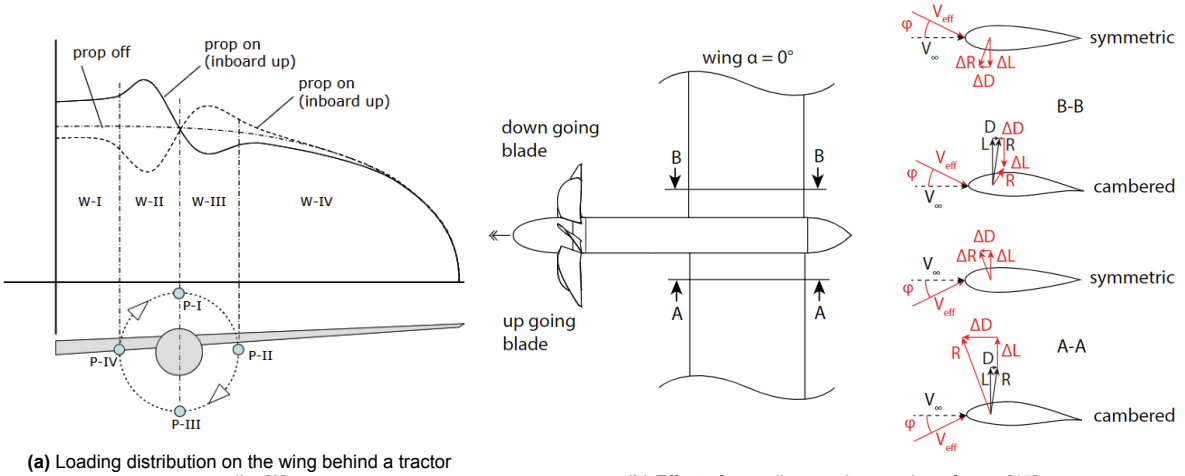

(a) Loading distribution on the wing behind a tractor propeller [9].

(b) Effect of propeller on wing resultant forces [15].

Figure 2.3: Comparison of loading distribution and effect of propeller on wing resultant forces.

In conclusion, having a tractor propeller will alter the lift distribution, and lead to swirl recovery. Both of these are effects due to the upwash and downwash at the respective sides of the slipstream. These effects are used in this thesis to verify the rotation direction and explain the lift loading in the results.

2.1.3. Tip-mounted propellers research background

Substantial research has already been done on the effects of wingtip-mounted propellers in different configurations and conditions. Efficiency benefits of wing-tip mounted propellers have been illustrated as early as 1969 by Snyder [16]. Since then, this theory has been tested in different set-ups and approaches. Although having co-rotating propellers is the standard practise in industry due to manufacturing costs, counter rotating propellers are considered for research to optimise the aerodynamics. An inboard-up rotating propeller at the wing tip reduces the drag of the wing [17]. Also, experimental results show that the swirl angle is reduced due to the presence of the wing [17, 14]. This would suggest that that energy is converted to useful thrust. Due to the opposite directions of the wingtip vortex and the propeller slipstream swirl, the wingtip vortex is attenuated. This results in an effective

aspect ratio increase of the wing, leading to a lift increase and a drag reduction [9]. Additionally, this rotation direction decreases the pressure drag coefficient of the nacelle [18]. Therefore, an inboard-up tip-mounted propeller is to be used.

2.1.4. Propeller vertical position research

The position of the tip-mounted propeller vertically is yet to be investigated further. Changing the vertical position of the propeller in an experimental set-up also modifies the mounting of the propeller and nacelle. So if done in the wind tunnel, it is a challenge to draw conclusions just on the propeller position. For that reason, the research discussed in this section that is already done, as well as the future research that is recommended, is done numerically and without mounting effects.

Using lifting line theory and inviscid compressible CFD, de Souza and Ciloni [19] show that the vertical position level to the wing has minimized induced drag. There are some limitations to this paper. The model in this paper always aligns the propeller with the incoming flow. This is not realistic, and Veldhuis [9] states that the installation angle of the propeller could lead to advantageous aerodynamic effects when it is aligned with the incoming flow.

According to Veldhuis [9], this shown minimum if the propeller is level to the wing is a local drag minimum. It is likely due to the area of the wing that is in the high dynamic pressure of the propellers. Instead, this is not where the dynamic pressure increase is biggest. The increase in dynamic pressure at the wing behind the propeller is illustrated in Figure 2.4. The grey area is the the area with the maximum dynamic pressure increase, due to the nature of the propeller blade loading. The figure shows $z_p \leq 0$, where z_p is the vertical position of the propeller, but the same applies for the propeller above the wing. Actually, Veldhuis concludes that a high vertical position is beneficial due to the increase in dynamic pressure and the local increase in wing angle of attack due to the slipstream contraction [9].

The primary focus of this thesis is to explore the impact of nacelle exclusion, which lays the groundwork for additional studies on propeller placement. Similar to the research in Braunchweig [8], the propeller position is very relevant. However, adjusting the vertical position of the propeller without it being mounted to the wing, makes it unrealistic. The tip vortex remains constant at the wing's location, which is beneficial for comparison purposes, but in reality, a mounting system would be in place. If a mounting system were utilized, it would result in the adjustment of several parameters, including the tip vortex and potential separation due to the modified shape. A fair comparison could be achieved if the nacelle is omitted in all vertical positions. Therefore, this report's research can serve as an initial step towards conducting research on vertical positioning by examining the nacelle's influence in these comparisons.

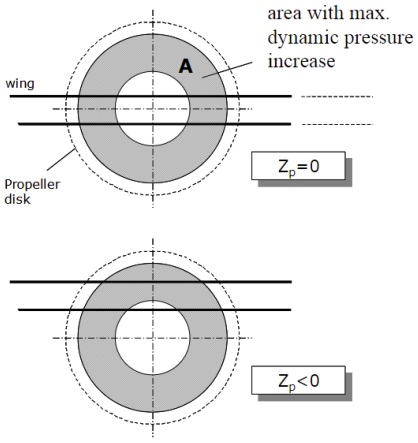

Figure 2.4: Increase in dynamic pressure over the wing at varying vertical positions [9].

In conclusion, there are two effects of the vertical position identified in research: the dynamic pressure increase and slipstream contraction. Further numerical research is needed, of which the first step is to investigate the effect of the nacelle as this is a prerequisite for research on propeller position.

2.2. Chosen numerical modelling methods

Numerical simulations are used in this research, as these are an addition to work done in wind tunnels. Using numerical simulations, assumptions made in the wind tunnel can be verified with more freedom in the set-up as the propeller does not need a propulsion system, and more can be visualised than feasible in a wind tunnel setup. In a wind tunnel setup the acquired data is limited, so with numerical

simulation a more detailed examination can be done. For example, in an experimental set-up Duivenvoorden observes the flow over the wing moving opposite to the main swirl direction [20]. It is believed that this is the effect of the root vortex system visualised, though it is recognised that this is potentially not the dominant flow characteristic. It is a disadvantage of this method for visualising slipstream interaction, because off-the surface flow characteristics are not visualised. With Computational Fluid Dynamics (CFD), a visualisation can be made of the whole flow field.

In addition to CFD, other numerical modelling tools are available, like the Lifting Line Theory (LLT) as used by de Souza and Ciloni [19], or the Vortex Lattice Method (VLM). However, with these lower order methods, viscosity is neglected [21]. This is undesirable for this research, as it is a recommendation in literature that viscosity should be included to be more accurate from a physics point of view and more applicable to a real world aircraft and wind tunnel experiments [19].

2.2.1. Computational Fluid Dynamics

The main tool used in this research will be Computational Fluid Dynamics (CFD). Anderson defines CFD as ”the art of replacing the integrals and partial derivatives in the governing equations with discretized values at discrete points in time and space” [10].

The CFD simulations will be performed using a 3D model that matches the geometry of the FutPrInt50 research. The accuracy and reliability of CFD simulations are dependent on the quality of the computational tools and models used, and the validity of the assumptions made about the flow field. In the literature study, research was done on common practises and guidelines, that lead to the choices made and be discussed in the set-up in chapter 3. Results from the CFD simulations are expected to allow better understanding of the flow phenomena of the propeller-wing system. This way, the development of the flow field can be analysed.

For propeller-wing interactions, the conclusion in research papers is that the Reynolds Averaged Navier Stokes (RANS) equations are capable of modelling aerodynamic interactions. Stokkermans concludes that RANS is good for the wingtip-mounted propeller in tractor configuration [22]. And also the thorough analysis by Taniguchi use compressible Navier-Stokes equations [18].

Turbulence models are closure models for the RANS equations. This is necessary because there are more unknowns than equations, and thus the turbulence model is used to approximate the fluctuating stress tensor [23]. It was chosen to model using the Spalart-Allmaras one-equation model. The Spalart-Allmaras one equation model solves one additional transport equation to determine the turbulent viscosity [23]. This makes it a robust and computationally efficient method, as it requires only one transport equation. In addition, it is the most common method used for propeller wing studies in the literature study, such as the similar applications by Stokkermans [22].

2.2.2. Propeller modelling with actuator disks

The propeller can be modelled by modelling the whole rotating geometry, or by replacing the propeller with distributions of momentum and energy sources representing the blades or the whole disk.

The decision for this study involves either repeatedly modeling the entire propeller geometry for each case or modeling it once and utilizing this model to apply a line or disk model for each simulation. By using an actuator disk or line model, subsequent simulations will require less computational power. However, the process may not necessarily be quicker as these additional steps also demand significant effort. Nonetheless, this method maintains consistent blade loading despite the wing’s effect, which is crucial as only vortex interactions are being examined. Additionally, the modeling of slipstream contraction continues. Ultimately, opting for a line or disk model is advantageous as it reduces both time and computational resources.

With an actuator line model, the propeller blades are replaced with distributions of momentum and energy sources representing the blade [22]. These distributions can be best guesses, something representable, or in the most accurate form the loading is applied from data of a full-blade model. The

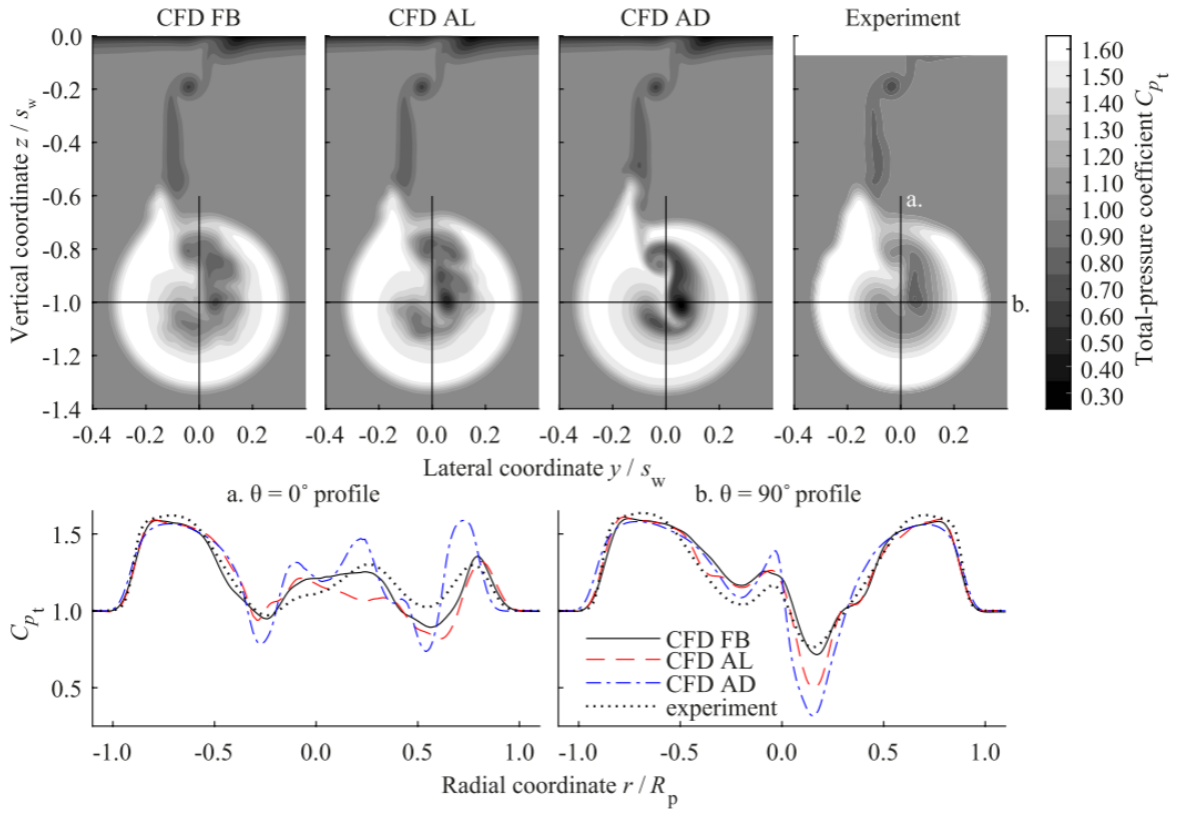

Figure 2.5: Validation study comparing a.o. actuator disk (AD) and full blade model: total-pressure coefficient at wake plane with flap deflection of 10°, from [22].

actuator disk model is similar, but then for the whole disk. Therefore, it can be solved as a steady problem. For that reason, an actuator disk model is chosen.

Research has shown that the actuator line and actuator disk models provide an accurate time-averaged slipstream [22]. As shown in Figure 2.5, the author concludes that the actuator disk ("CFD AD") model provides an accurate time-averaged slipstream. The differences present are attributed to the differences already present in the isolated propeller due to numerical diffusion in the vortex cores. Therefore, for within the model, taking the same typical loading distributions in each case could lead to a solid experiment. The source of error present would be compared to the full blade model or an experimental model, though based on Figure 2.5 the actuator disk gives results close to the full blade case.

Blade loading in this thesis will be extracted from propeller modelling done in a similar case [24] but this will be further discussed with the set-up of propeller modelling in subsection 3.2.2.

3

Model

In this chapter, first the methodology is discussed and then the set-up, after which dependency studies are done. In the methodology in section 3.1, the steps taken in this research to answer the objective are explained. Then, in section 3.2 the information discussed before is used to set up the numerical model. In subsection 3.2.1, 3.2.3, 3.2.5, and 3.2.4 the choices made for the geometry mesh, turbulence set-up, and boundary conditions are discussed. This is very relevant for the correctness and replicability of the results. In subsection 3.2.2, the propeller disk model is explained. And finally, in section 3.3, part of the validation is done by a domain dependency study and a grid dependency study.

3.1. Methodology

In order to investigate the effect of the presence of the nacelle on the aerodynamic performance, four configurations are used: with and without nacelle, and with and without propeller. These are labelled below:

- Wing only: 'w'
- Wing and nacelle: 'wn'
- Wing, nacelle, and propeller: 'wpn'
- Wing and propeller: 'wp'

Using these four configurations, the research questions as described in the introduction are to be answered. In Figure 3.2 a summary of this process is displayed. First, the effect of the nacelle presence is investigated without the propeller installed yet. This is labelled "Compare 'w' with 'wn'", and the performance parameters and other installation effects are looked at. Then, the same is done with the propeller installed, comparing 'wp' and 'wpn' to see what the effect is of adding the nacelle when the propeller is on. Lastly, the effect of the nacelle on the propeller addition characteristics is investigated.

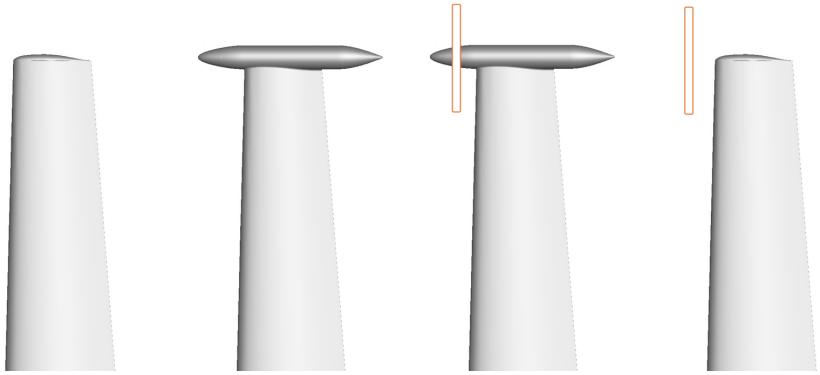

Figure 3.1: Configurations used, left to right: 'w', 'wn', 'wpn', and 'wp'.

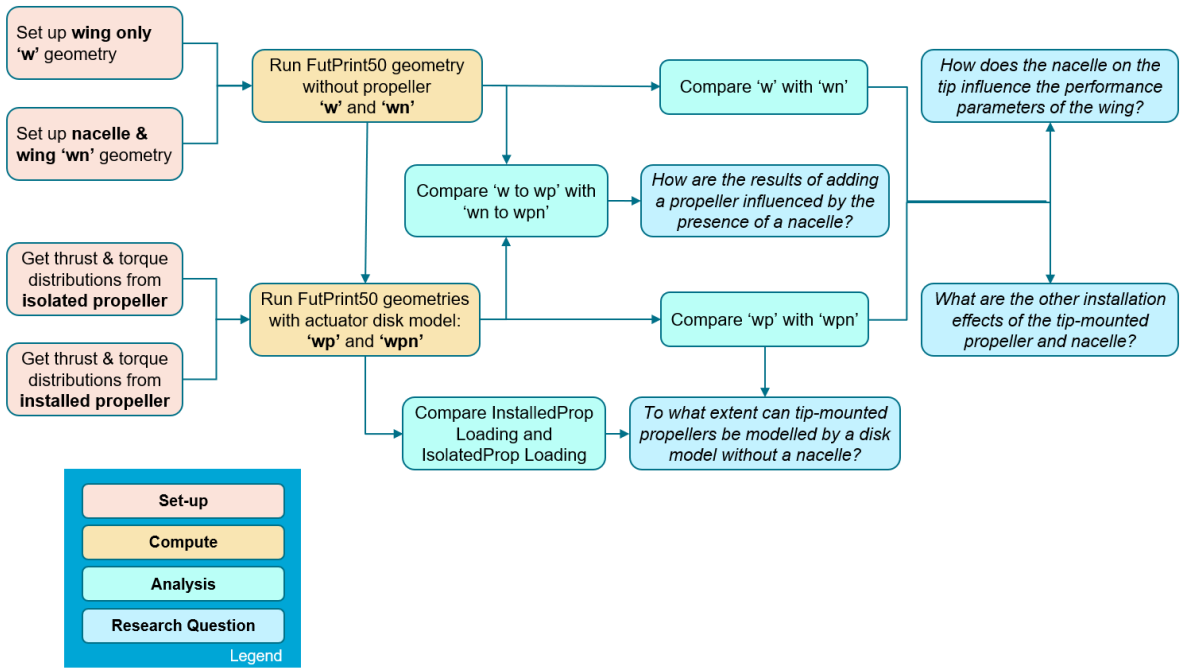

Figure 3.2: Method diagram for this thesis.

This is done by comparing the effect of adding the tip-mounted propeller, with and without nacelle: "Compare 'w to wp' with 'wn to wpn'".

Furthermore, as the propeller is modelled by an actuator disk (AD), the impact of the choice of loading distribution on the wing performance is investigated. This step is called 'Compare InstalledProp Loading and IsolatedProp Loading' in Figure 3.2. The disk model loading is taken from two simulations done by J. Goyal [24]. These are discussed in subsection 3.2.2, and summarised below:

- Installed propeller data. Here the propeller was modelled in front of a wing, so the wing has an influence on the propeller loading, as described in subsection 2.1.2. Because this set-up is similar to the geometry modelled, this is the expected loading for this case as well. This case is also referred to as 'InstalledProp Loading'.
- Isolated propeller data. Here no wing is present. Ideally, the isolated data could be used when the disk model is moved in space, such that the loading is not affected by the wing placement. This case is referred to as 'IsolatedProp Loading'.

From this comparison, the IsolatedProp Loading is chosen to work with for the other steps. At a later stage, the geometry of the wing is changing as the nacelle is removed, and the propeller might be moved upstream. For this reason, the isolated data is more universally accurate. The results of this step will show to what extent using the isolated data in the disk model in later steps is not precise and help answer the question "to what extent can isolated propeller loading be used in a disk model for tractor tip-mounted propellers?".

3.2. Set-up

The numerical set-up is inspired by the wind tunnel experimental simulations. The cross-section of the test section as well as the operating conditions are matched with the DNW-LST. The DNW-LST has an operating range of 0-80 m/s [25], though the experimental research is conducted at a maximum of 60 m/s, so that value is chosen. The operating conditions are summarised in Table 3.1.

Condition	Value
Angle of attack wing (α)	$0°$
Inlet velocity (V_{inf})	60 ms^{-1}
Mach number (M)	0.17
Angle of attack propeller (α_{prop})	$-3.5°$

Table 3.1: Operating conditions for simulations.

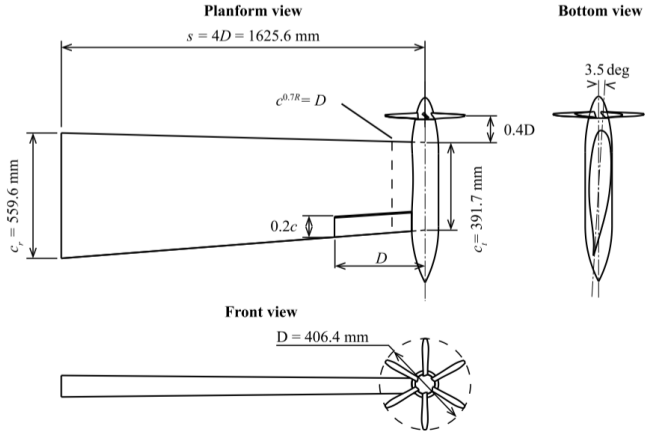

Figure 3.3: Geometry of the wing and nacelle.

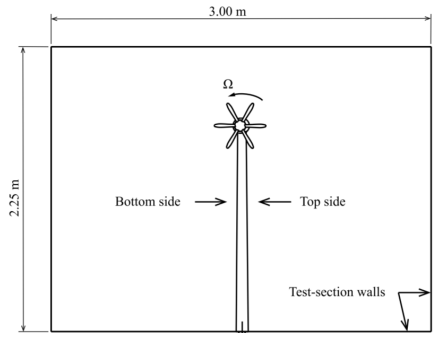

Figure 3.4: Cross section of the DNW LST wind-tunnel.

Figure 3.5: Experimenal set-up for reference values [26].

3.2.1. Geometry

The geometry and domain for this study is matched to the experimental research for FutPrInt50 as much as possible. With the numerical modelling the aim is to find if assumptions made in the wind tunnel work for experimental set-up. For this reason, the domain and locations of data processing are based on the experimental set-up.

The cross-section of this domain can be seen in Figure 3.4. Also the propeller data, as discussed in subsection 3.2.2, will have the showing rotation direction with inboard-up. The wind tunnel walls are wall boundaries in the flow domain of the model. However, in the simulations this cross-section is constant throughout the length of the tunnel. In length, the location of the inlet and outlet are studied in the domain dependency study in subsection 3.3.1, leading to an outlet length of 20 MAC and an inlet length of 15 MAC.

The model file of the wing is obtained from the experimental simulations as well. From the 3D files, all holes are removed and the aileron is filled up, to make it smooth enough for meshing. In this research, one geometry with the propeller and one geometry with a wingtip instead is used, as shown in Figure 3.1. The propeller blades are not included because only actuator disk simulations are performed, but the location where the blades are attached to the nacelle is taken from the model and used in subsection 3.2.2. The wing has zero angle of attack, the chord is aligned with the wind tunnel walls and thus the direction of flow. The nacelle has a negative angle of attack, as it is pointing downwards in the geometry. The nacelle tilt angle of 3.5 degrees is also verified in the 3DEXperience model.

3.2.2. Propeller modelling

The propeller in all the simulations is modelled with a disk model. This model represents the loading of the propeller blades by a propeller disk. This loading distribution is time-averaged throughout the disk. Therefore, this still takes into account the radial and azimuthal variations in loading, but it can be solved as a steady problem. This method was chosen because it is easier to simulate without the time-dependency, as was discussed in subsection 2.2.2.

The disk model is given to fluent by a user defined function (UDF). The load of the disk model is in radial coordinates, with a tilt of -3.5 ° and going opposite to the tip-vortex (anti-clockwise). The location of the center is placed where the propeller would also be mounted in the model. The analysis of the input data is done below, where also the differences between the installed and uninstalled data are identified. Then, the orientation in the model is verified.

Input data

Using the disk model, the relative position of the propeller and the wing can be changed easily, and in future research it is desired to change the vertical position of the propeller. Therefore, the wing's influence on the propeller's load is investigated first by using installed & isolated propeller loading data. These loading cases can be seen in this section.

This data is the result from CFD analysis on a similar, but not exactly geometrically the same, wing [24]. The isolated and the installed loading case do have the same conditions, and are summarised in Table 3.2. The propeller loading simulations are done under a negative angle of attack of 1.5°, so tilted forward. The simulations are done with a free stream velocity of 60 m/s [24], which is the same as the operating conditions used in the model for this thesis. The operating conditions for the input data is given in Table 3.2, while the operating conditions for the simulations in this thesis is given above in Table 3.1. It can be seen that in both geometries the nacelle and propeller are attached to the wing with a 3.5 ° tilt. However, for the input data simulations, the whole geometry was tilted 2° such that the with has a positive angle of attack and the magnitude of the propeller angle of attack is reduced to 1.5 °. In an ideal scenario, it would be more accurate to ensure the alignment of these angles, which would mean rotating the geometry in this thesis simulation as well. However, this is not done. This study aims to compare the installed and isolated cases, and to examine the impact of the propeller's load on the nacelle's installation effects. Therefore, the deviation of this load that is expected from 2 degrees angle of attack does not significantly undermine the validity of the research findings. The loading distributions can be seen in Figure 3.6, where the wing would be on the right side of the page.

Condition	**Value**
Angle of attack wing (α)	2°
Inlet velocity (V_∞)	60 ms^{-1}
Angle of attack propeller (α_{prop})	-1.5°
Advance ratio (J)	2
Propeller pitch	25°

Table 3.2: Operating conditions for input data.

The data in these figures are the sectional thrust and power coefficients. For the disk model, the sectional thrust and torque are needed. To get these, Equation 3.1 and Equation 3.2 are used, where n is the rotational speed.

$$T = T_c'(\rho \cdot V^2 \cdot D) \qquad \text{and} \qquad P = P_c'(\rho \cdot V^3 \cdot D) \tag{3.1}$$

$$Q = \frac{P}{2\pi n} \qquad \text{where} \qquad n = \frac{V_\infty}{J \cdot D} \tag{3.2}$$

It can be observed in the input loading figures in Figure 3.6 that the loading is asymmetrical and also the effect of the wing on the installed loading can be observed. The loading is asymetrical in all cases due to the angle of attack, this is already seen in the isolated loading in Figure 3.6a and Figure 3.6b. Due to the angle of attack, the propeller is tilted forward and the relative velocity of the upgoing blade is increased. This leads to a higher blade loading for this upgoing blade, which is at the inboard location. The installed loading in Figure 3.6d and Figure 3.6c is affected by the wing behind the propeller. Due to the blocking of the wing, which is only on the right side as it is tip-mounted, this is expected to locally

lead to a higher loading. This is difficult to see because the loading is already asymmetrical. Furthermore, due to the circulation induced velocities the overall velocity on the pressure side of the wing goes down, also leading to higher loading. In front of the wing the upgoing blade would have more thrust, which is also on the inboard side. This is why in Figure 3.6c and Figure 3.6d it can be observed that below the wing the loading is the highest. Since the loading is different in each case, the integrated thrust and torque coefficients are also given. These are a reference for the total differences seen in the results. The integrated thrust and torque are given in the caption of the figures in Figure 3.6, these are along the propeller axis and using Equation 3.1.

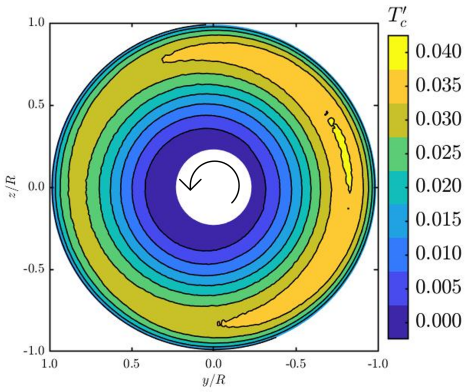

(a) Isolated propeller thrust distribution, $T_c = 0.0397$.

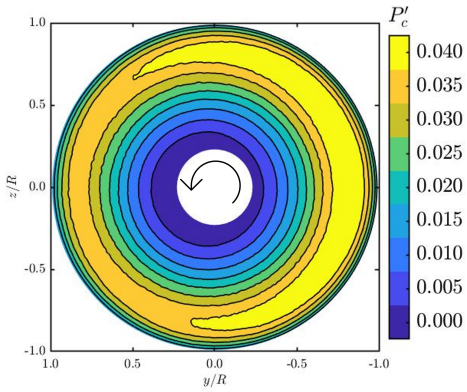

(b) Isolated propeller torque distribution, $P_c = 0.0503$.

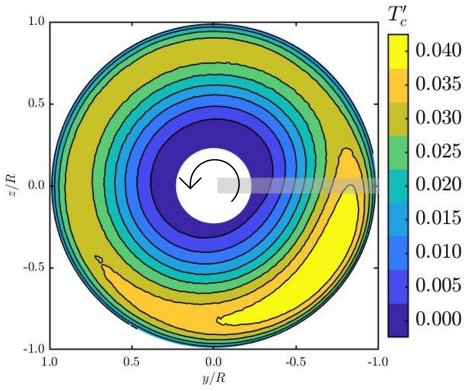

(c) Installed propeller thrust distribution, $T_c = 0.0404$.

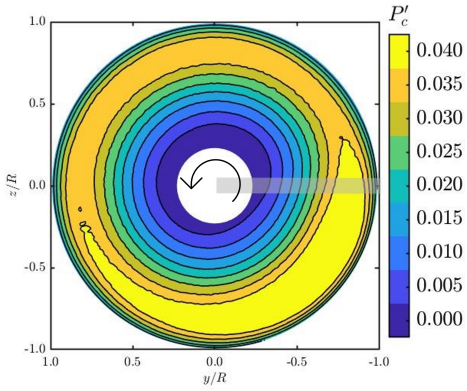

(d) Installed propeller torque distribution, $P_c = 0.0513$.

Figure 3.6: Loading used as input for Loading 1 (installed) and Loading 2 (isolated) case [24].

Orientation

As the disk model is implemented numerically, a verification is done to see the result of this set-up. For this, the pressure just behind the propeller disk is plotted, and should look similar to the input data. Also, geometrically, the tilt can be shown in the model. And finally, the rotation direction is verified.

The input data as discussed in subsection 3.2.2 is asymmetrical, therefore it is important that the rotation of this disk is implemented correctly. This is verified by plotting the pressure coefficient just behind the implemented propeller disk. The total pressure coefficient increases with higher loading, so the distribution can be directly related to the input data. In Figure 3.7 the loading just behind the disk is seen for the installed case, and it is visually observed that with the maximum loading inboard under the wing this is at the correct quadrant. Thus, these settings ensure the implementation is in accordance to the input data.

This pressure distribution in Figure 3.7 is compared with the loading in Figure 3.6 to observe that the highest load is inboard under the wing, as expected. Also, it can be observed that the propeller has a tilt in the same direction of the nacelle. Knowing it has a tilt of 3.5 $^\circ$, it was ensured that the propeller

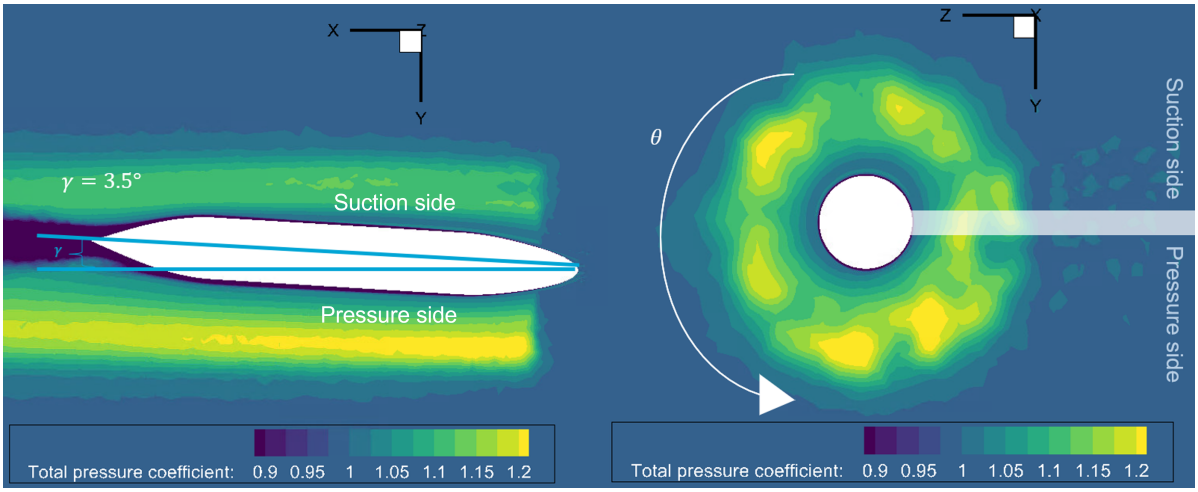

Figure 3.7: Total pressure for qualitative analysis of rotation, location and tilt.

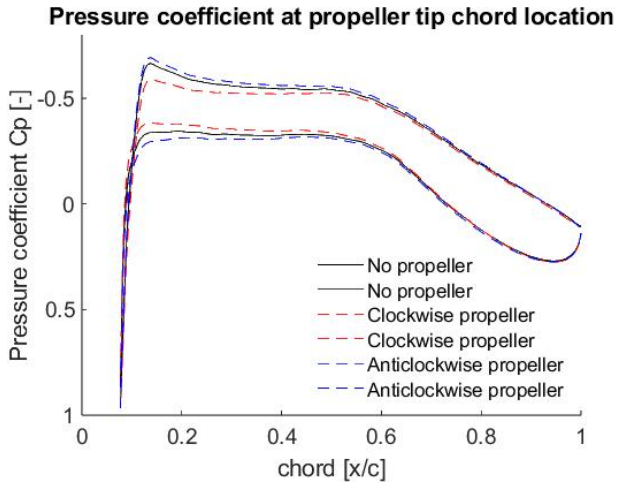

(a) Pressure coefficient over the chord comparing clockwise and anti-clockwise rotating propeller set-up.

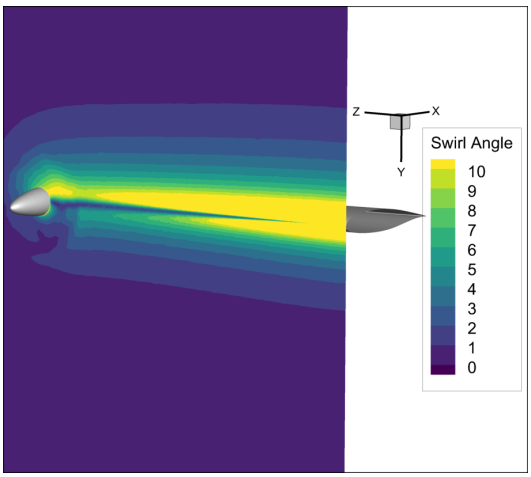

(b) The swirl angle at a plane in front of the wing and behind the disk model [deg], x=0.

Figure 3.8: Results of clockwise and anti-clockwise propeller rotation.

axis implemented has the expected tilt in the right direction.

Lastly, the direction of the rotation is verified. The model is implemented such that the propeller in opposite direction to the tip vortex. The rotation is flipped by flipping the sign of the torque in the inlet data. Due to the conversion of the momentum, the sign of the torque determines clockwise or anticlockwise rotation. By running both cases, with clockwise and anti-clockwise propeller rotation, the local lift increases and decreases as expected. This was seen by the lift distribution on the wing, and local pressure over the chord, as the local lift was lower than without the propeller. This corresponds to the propeller-wing interaction theory, as the local angle of attack is reduced by the slipstream from the propeller and thus the local lift is decreased. This effect is shown in Figure 3.8a. This corresponds to the theory in chapter 2, looking at the intersection between W-I and W-II in Figure 2.3a.
Also, the swirl angle is expected to decrease if the rotation direction of the propeller is opposite to the tip vortex, as is required. And it would increase when the rotation direction is in the same direction of the tip vortex. While the maximum swirl angle by the wing tip vortex without a propeller present is 3.4 degrees at 2.5 MAC behind the wing, with the clockwise rotating propeller this is increased to 5.8 degrees, and with the anticlockwise rotation it is reduced to 2.8 degrees. With these measures, it was ensured that the rotation direction is opposite to the tip vortex direction, so inboard-up.

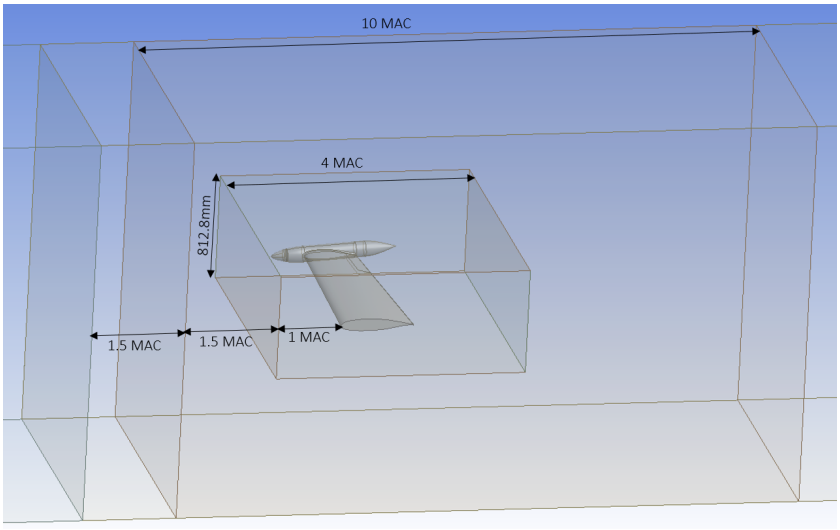

Figure 3.9: Computational domain around the refinement boxes.

3.2.3. Computational domain

Defining the mesh in the domain is crucial for the research outcomes. To be able to simulate well, the mesh needs sufficient refinement, while at the same time the resources are limited, so the simulation has to be as efficient as possible to save time. This section is about the choices made in defining the mesh, and in subsection 3.3.1 the refinement is tested and chosen.

Around the wing the cell size needs to be the smallest, as the highest pressure gradients are expected around the geometry and in the wake behind it. Also, the mesh always needs to be as smooth as possible for numerical stability, such that the flow is not hindered by discontinuities in the mesh. Thus, the steps in growth in cell size are gradual. For this, the tool 'Body of Influence' is used, leading to a smoother gradient between the refinement in the different boxes.

The domain is split up into the far upstream, far downstream and two refinement boxes. The finest region is a box enclosing the wing, based on the parameters used for RANS research before [22], with the width of two propeller diameters. In the length, span direction, this box goes from wall to wall of the wind tunnel domain. The boxes around the wing can be seen in Figure 3.9. Note that the measurements in the wake will be done at 1.5 MAC behind the wing, so within the finest box. Furthermore, the wing surfaces are refined even further using face meshing, with which also the trailing edge and nacelle are more refined in order to account for the curvature in the geometry.

Around the wing and nacelle, an inflation layer is made to better simulate the boundary layer. The inflation layer around the geometry is there to ensure that the boundary layer is fully resolved. The y+ value is a dimensionless parameter, and it is standard practise for the SA turbulence model to aim for a value below 1, which is thus used as input in Equation 3.3. To find the first layer thickness with this equation, first the skin friction Cf is estimated with the Reynolds number in Equation 3.4, from which the wall shear stress (τ_w) and thus the frictional velocity (V_τ) is calculated in Equation 3.5 and 3.6. The Reynolds number is calculated with the variables used for the experimental set-up and the standard atmosphere. The first layer height (dy_1) is then calculated using these parameters [27]. With the first layer height and an assumption for the growth rate of the layer heights, the number of layers is calculated such that it smoothly transitions into the next meshing grid.

$$dy_1 = \frac{y^+ \cdot \mu}{\rho \cdot V_\tau} \tag{3.3}$$

$$Cf = (2 \cdot log_{10}(Re_c) - 0.65)^{-2.3} \tag{3.4}$$

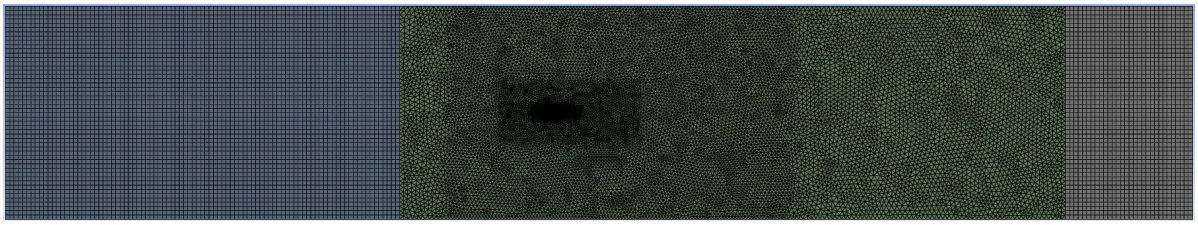

Figure 3.10: The computational domain as seen from the side (z).

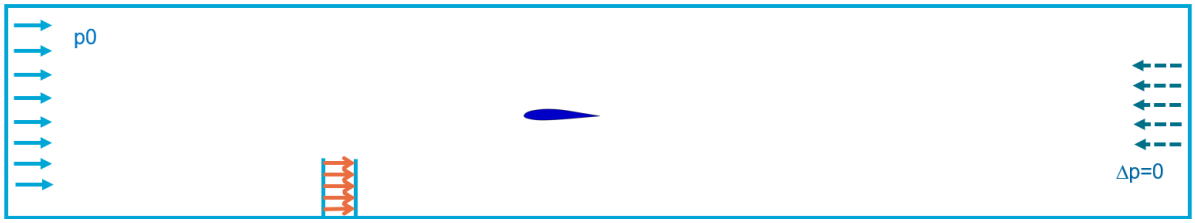

Figure 3.11: Boundary conditions computational domain, showing pressure inlet and outlet, and slip walls of the wind tunnel.

$$\tau_w = 0.5 \cdot Cf \cdot \rho \cdot V^2 \tag{3.5}$$

$$V_\tau = \sqrt{\frac{\tau_w}{\rho}} \tag{3.6}$$

All meshing in the inner domain is modelled with tetrahedrons, as it is the fastest way to generate a mesh that requires the least amount of memory [23]. Only the far upstream and downstream are meshed with blocking, so in hexahedrons. This saves computational cost, whilst it is not expected to affect the results. Also the tetrahedron cells could be transferred to hexahedron and polyhedron cells, but this turned out to be out of the scope of this research. The upstream part is the inlet flow developing, which can be modelled well with blocking, and the downstream blocking is also far behind where the measurements will be taken place. In subsection 3.3.1 the effects of the inlet and outlet location are investigated. The computational domain can be seen in Figure 3.10.

The quality of the mesh is checked visually and computationally. Visually, it can be observed if the ratio's between the blocks are too high, these should be smooth. With the analytics in the mesh software, the quality of the mesh can be checked by looking at the key performance indicators: aspect ratio (AR), skewness and orthogonal quality of the mesh. The orthogonal quality should be as high as possible, with the minimum value greater than 0.1, the skewness should be as low as possible, meaning the faces and cells are more ideal, with the maximum lower than 0.9. Lastly, the aspect ratio should be lower than 10, when the AR is 1 the grid consists of squares, which is best for computation. These values are based on the ANSYS User's guide [28]. In the meshing, the cells with a specific mesh quality value can be selected, and thus adjusted. For example, in the first mesh grids, the orthogonal quality was lowest at the trailing edge of the wing, meaning it should get some refinement.

3.2.4. Boundary conditions

To model the domain well, the boundary conditions need to be specified. The inlet and outlet have the fluid go through them, and need to account for the velocity and pressure change at that location. The geometry and the wind tunnel walls are physical boundary conditions, where the flow does not cross the wall, but their properties need to be modelled as well.

Inlet and outlet

The inlet and outlet boundary conditions are pressure boundaries. The model in general needs the energy equation to be turned on, such that the thermal properties can also be given. For the rest, stan-

dard atmospheric conditions at ground level are used as this would represent the wind tunnel.

The gauge total pressure is the difference between the total pressure at the static pressure. The static pressure is 101325 Pa, standard static pressure. And the total pressure is calculated with this, the specific heat ratio of air of 1.4, and the Mach number, using Equation 3.7.
Eventually, the settings used are as follows. The reference temperature used is 300K, giving a total temperature of 301.79K, for the inlet and for the outlet. The gauge total pressure is 2134 Pascal. And the supersonic initial gauge pressure is ignored for subsonic flow.

$$p_0 = p_{stat} \cdot (1 + \frac{k-1}{2} \cdot M^2)^{(\frac{k}{k-1})} \tag{3.7}$$

Lastly, for the outlet, the gauge pressure given is zero. Since there is no additional pressure except for the atmospheric pressure equal to the static pressure in the model, the gauge pressure at the outlet is zero. No pressure differences are induced here. Also, no back flow is expected at the outlet.

Walls
As for the walls, for the model a no-slip boundary layer is applied as the developing boundary layer is essential for the results. And for the wind tunnel walls, a slip boundary layer is applied to all walls.

For the wind tunnel walls it is a simplification made that there is no-slip on the wind tunnel walls, as in reality there is a boundary layer developing there. The disadvantage of using slip is that at the wing junction this ignores the interaction effect between the wall boundary layer and the wing. Changing the loading at the root of the wing due to this boundary layer can affect the loading at the tip, but the assumption is made that this effect is relatively small. With the geometry and operating conditions of this simulation, the boundary layer at the root is not of interest. Also, it is an additional challenge to model the no-slip while the boundary layer does not get too big and interferes more with the results than the experimental set-up does. Therefore, all the wind tunnel walls are modelled with a slip boundary condition.

3.2.5. Turbulence modelling

Like explained in chapter 2, turbulence models are closure models for the RANS equations. For each turbulence model, often the turbulence intensity and a viscosity ratio are required, to determine these quantities is quite complex. So the values can be taken from best practises in the field. The viscosity ratio is usually between 1-10, and the turbulence intensity is in the order of 0.1% [23]. The turbulent viscosity ratio is found with $\frac{v_t}{v} = 2 \cdot 10^{-7} \cdot Re_c$ [29]. Also, the turbulence intensity used is 0.1% [29]. The viscosity ratio has to be done right, as they have a strong influence on how the turbulence develops. Therefore, if the turbulence decay is too strong or not rapid enough, this viscosity ratio can be edited in the settings. This was not necessary for this research, as this proposed equation gave a well working ratio of 0.34.

3.2.6. Convergence

The set-up and settings are chosen to avoid divergence, but in addition convergence has to be confirmed and checked.

A density-based solver is used, so the governing equations are solved simultaneously. Only other scalars such as turbulence is solved separately. Furthermore, an implicit method is chosen, meaning the parameters at the nodes are calculated using estimated values at the neighbouring nodes. For the Courant number (CFL), a CFL of 5 is chosen. The CFL is a condition for the time step of the scheme. A higher Courant number leads to a faster information propogation, but may lead to an unstable result. So, if the solution is diverging, the CFL can be lowered. It is advised to use a Courant number (CFL) of 5 for this method by the user guide [30].

With the simulations done, the rate of convergence is observed. This results in all the runs done with 1000 iterations. After each run, it is important to manually check if the case has a sufficiently

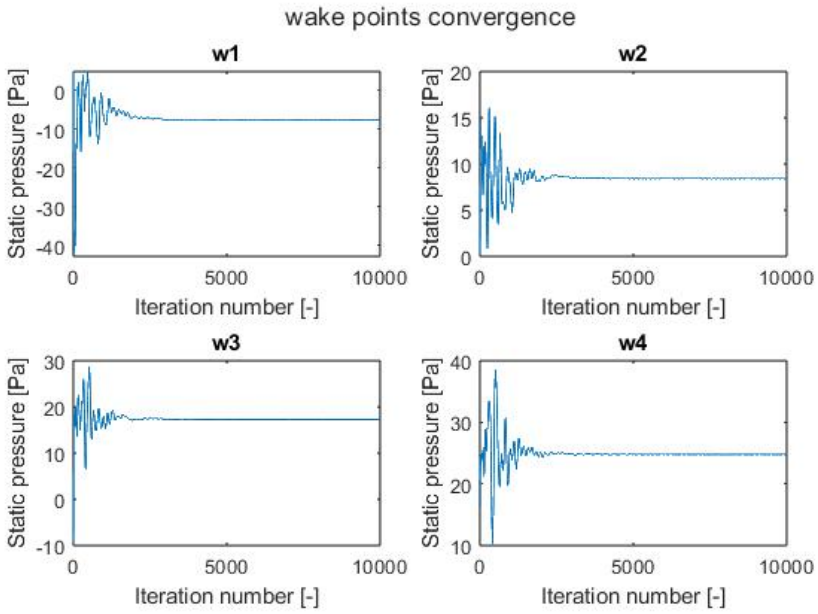

Figure 3.12: Convergence of wake pressure points.

converged solution. This is done by plotting parameters at each iteration: showing the lift, drag and pressure points just in front and just behind the wing. These points are four evenly distributed on the span: at 0.4064m, 0.8128m, 1.2192m and 1.6256m. The points in front of the wing are at a streamwise position of 0, where the wing root leading edge is located. And the wake points are at a streamwise position of 1.2m, 2.5 MAC downstream from this leading edge. These points are chosen to make sure that in addition to the integrated values, the flow field around the wing especially is well-developed.

First of all, it should be observed that the value is converging with increasing iterations in Figure 3.13. The allowed error or uncertainty at the end should be negligible compared to other uncertainties in this research. For the dependency studies, the convergence plots are compared with each other. For the lift, drag and pressure convergence, the oscillation is looked at as a percentage of the final value. For example, the convergence for the wing, and propeller without the nacelle looks like Figure 3.13. In Figure 3.13c and Figure 3.13d the last 1000 iterations are shown. From this data, qualitatively it can be seen that the values oscillate but also the maximum error can be calculated, defined as the difference between the average value and the maximum difference. In this case, that would be 0.05% for the drag and 0.0002% for the lift. In all of the cases, this uncertainty is well below the set threshold of 0.1%, which is concluded to be tolerable compared to the other uncertainties. Checking the convergence is the first step in verifying the results, making sure the run went well. When the convergence does not look right, there are settings that should be adjusted.

3.2.7. Adjustments

With the disk model added, the set-up had trouble converging. Due to this divergence, the mesh had to be improved. This was done by locally improving the orthogonal quality, and refining the inflation layer of the wing.

In the results, it is observed that when the forces from the disk model are increased to the Futprint50 case, the y^+ value at the tip exceeds 1. This suggests that the mesh in the boundary layer is not fine enough. The first layer thickness is calculated with the inlet velocity, but the propeller also adds velocity to the flowfield. Locally, the velocity is up to 80 m/s. Therefore, a new first layer thickness is calculated with this value, changing it from $6.5e^{-6}m$ to $5e^{-6}m$. Also the corresponding number of layers are adjusted.

Furthermore, the orthogonal quality is identified as a leading cause of the divergence. The lowest quality was around the sharp edges in the trailing edge. Therefore, the geometry is slightly adjusted with

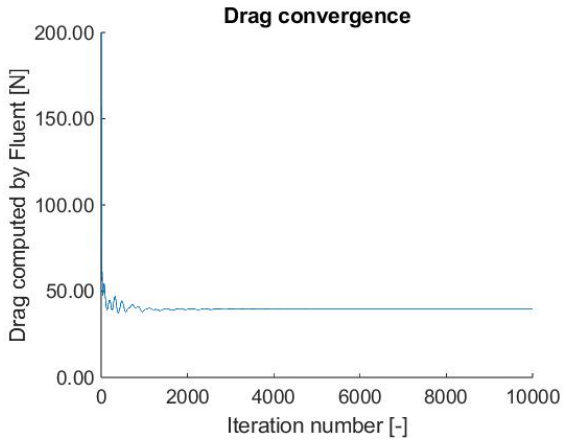

(a) Convergence of the drag given by fluent.

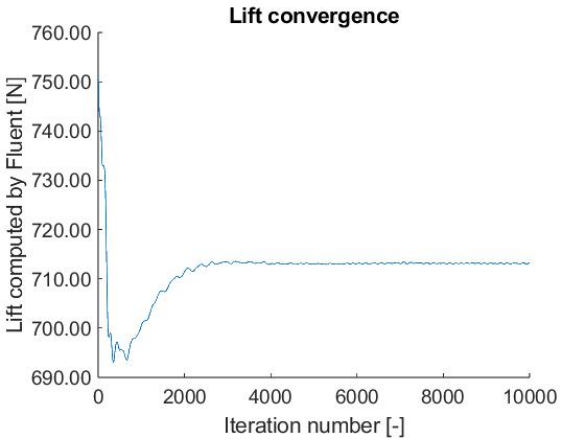

(b) Convergence of the lift given by fluent.

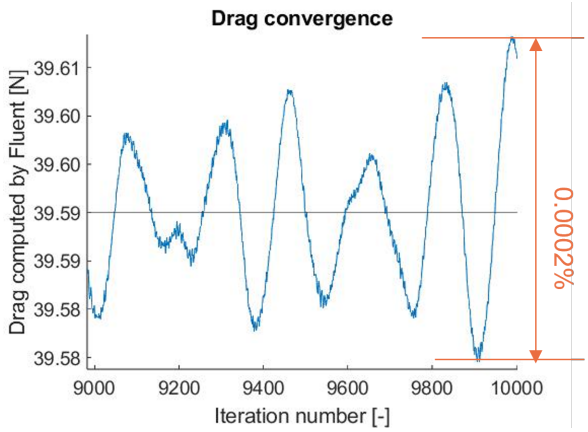

(c) Zoomed in, last 1000 iterations, convergence of the drag.

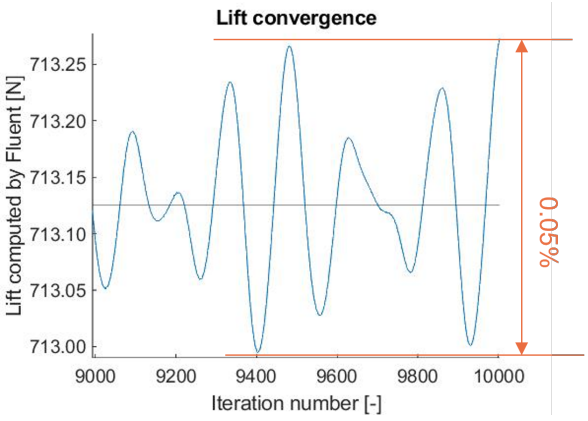

(d) Zoomed in, last 1000 iterations, convergence of the lift.

Figure 3.13: Some of the relevant convergence plots for one case (case 4), as an example of the validation done.

fillets to improve the orthogonal quality.

Due to these adjustments, the case converges well and data processing can be proceeded. However, at this point in the process the dependency studies have already been done. Due to restricted time, the dependency studies are not redone, and the following section are the results of the dependency studies on the original mesh.

3.3. Dependency Studies

In order to verify the set-up settings, two dependency studies are done. With these studies, the chosen set-up is tested by altering the parameters. First, a domain dependency study is done, checking the effect of the inlet and outlet position of the domain. Then, a grid dependency is done, checking the effect of the fineness of the grid and also estimating the error for the chosen grid size.

3.3.1. Domain dependency

For the domain dependency, both the inlet and outlet locations are altered. These are the boundary conditions of the domain. The length until the inlet or outlet should not affect the results of the simulations. However, if the boundary of the domain is too close to the object, it could be that this disturbs the calculations in the simulation. Table 3.3 shows the chosen domain dimensions. The inlet is varied between 15 and 20 MAC and the outlet is varied between 20, 30 and 40 MAC.

ID	Inlet [MAC]	Inlet [m]	Outlet [MAC]	Outlet [m]
1.3	15	7.2	30	14.4
1.5	20	9.6	30	14.4
2.5	20	9.6	20	9.6
2.6	20	9.6	40	19.2

Table 3.3: Domain dimensions for dependency study

All the runs are given 10 000 iterations, and convergence is checked. Then, the cases are evaluated separately to see if the results make sense.

The lift coefficient of this case with three different inlet lengths are 0.207215 and 0.207141 respectively for 20 and 30 MAC length between the wing and the inlet. The difference between these lift coefficients is 0.035%, which is an acceptable difference. Therefore, the smallest domain possible is chosen: 15 MAC lengths to the inlet.

For the outlet runs, the same analysis is done, while keeping the inlet at 20 MAC. The output graphs are also very similar. However, there is a pattern that the results from the 30 MAC case are notabily more distant from the 20 and 40 MAC case results. For the lift coefficient, this results in a 1.4% difference. Also in the lift distribution on the span this can be clearly be seen, as illustrated by Figure A.1a and Figure 3.17b. Though for the local lift coefficient, the difference is 0.6%. However, for the drag distribution, this clear effect can not be seen.

The outcomes of the inlet dependency are all similar, both visually and quantitatively. Since the differences are all maximum tenths of percentages, This range falls within an acceptable margin of error, as such uncertainties are deemed negligible in relation to the precision of the results. Therefore, for the final configuration an inlet length of 15 MAC (7.2m) can be used. Also for the outlet dependency, the differences are very small. The biggest error was found for the 30 MAC case, though also only still 1.4%. For this reason, the domain with 20 MAC outlet length is chosen to be sufficient and requires the least resources as well.

3.3.2. Grid dependency

With the chosen domain, a grid dependency study is applied. With this, the chosen fineness of the grid is tested. The goal is to get reliable results with the lowest computing time possible. The grid dependency study is done on the geometry with the wing and the nacelle, because if the grid is reliable

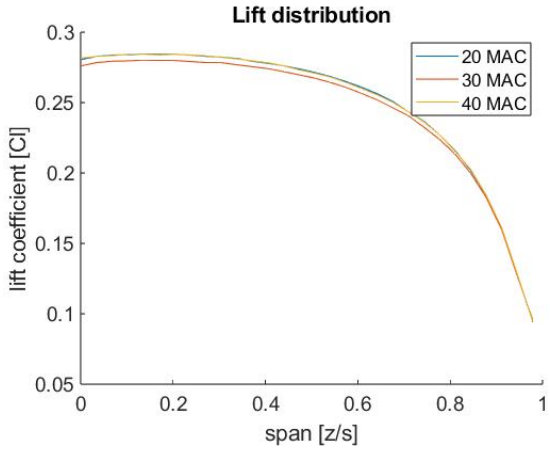

(a) Span lift distribution.

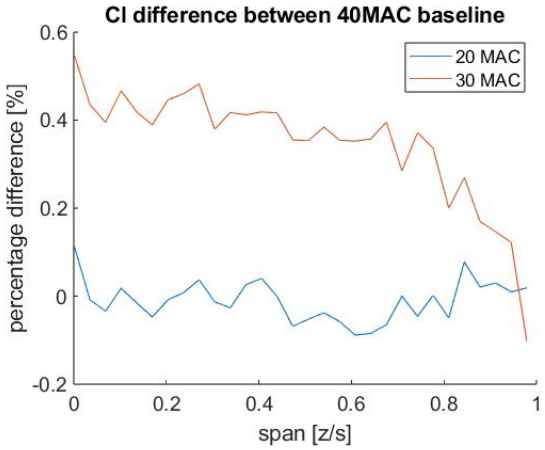

(b) Lift distribution relative difference.

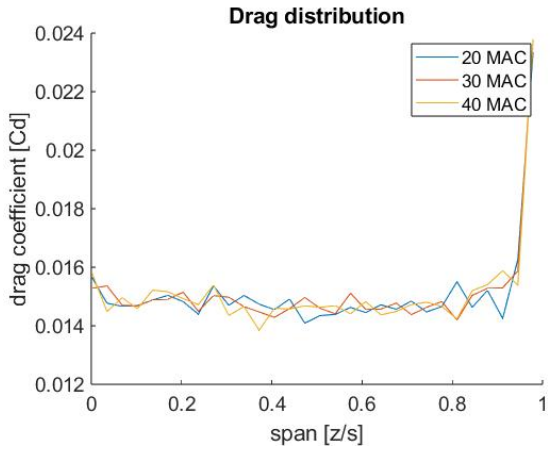

(c) Span drag distribution.

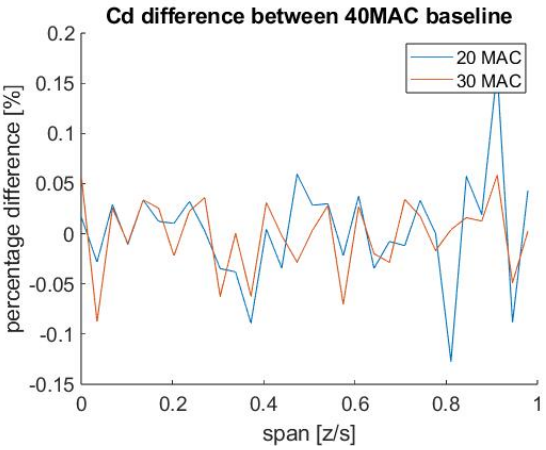

(d) Drag distribution relative difference.

Figure 3.14: Outlet dependency study results.

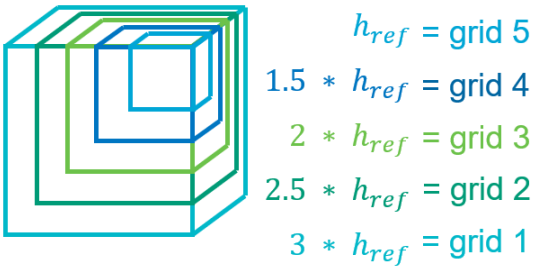

Figure 3.15: Grid sizes ratio, size of blocking.

with the nacelle it is assumed to be good enough with just wing as well and not necessarily the other way around.

To accomplish this, the mesh grid size is compared in both directions. Therefore, one coarser grid than the original grid is chosen, and three finer grids. With the finer grids it is tested if the results are reliable, and with the coarser grid it is tested if the grids are efficient and coarse enough. The difference between the grids is 20 %, as this is also the range used by Stokkermans [22]. This is illustrated in Figure 3.15. The ratios between the grid sizes of the different area's are kept the same. This is shown in Table 3.4. The sizes are in meters, where h_{ref} equals the blocking size of grid 5, so 0.04m.

Mesh region	ratio	grid 1	grid 2	grid 3	grid 4	grid 5
Blocking	Blocking	0.12	0.1	0.08	0.06	0.04
BOI 1	0.75 Blocking	0.09	0.075	0.06	0.045	0.03
BOI 2	0.66 BOI 1	0.06	0.05	0.04	0.03	0.02
Face wing	0.1 BOI 2	0.006	0.005	0.004	0.003	0.002
Face TE	0.02 BOI 2	0.0012	0.001	0.0008	0.0006	0.0004
Nacelle	0.04 BOI 2	0.0024	0.002	0.0016	0.0012	0.0008

Table 3.4: Mesh fractions and grid sizes [m] for the grid dependency.

The result of these runs are to see how much different the results are, and with that how accurate the final choice of grid is. A standard deviation is computed in Table 3.6, which will be kept in mind when analysing the final results of this thesis. Furthermore, the time to converge is noted, since this grows exponentially with the refinement of the grid. In order to quantify the comparison, the following quantities are looked at: C_l, C_d, and Cp_{min}. These are chosen as they are crucial outcomes of the tests. Also, Cp_{min} is expected to be most effected when the grid size is altered.

Grid	No. nodes	Total transcript time	Cl	Cd	Cp_{min}
Grid 1	3,779,915	12 h 3 min 26 sec	0.26976	0.0162	0.9460
Grid 2	5,312,176	16 h 21 min 41 sec	0.2695	0.0160	0.9343
Grid 3	8,183,204	26 h 6 min 52 sec	0.270723	0.01604	0.9185
Grid 4	14,141,679	44 h 8 min 13 sec	0.2700	0.0158	0.8784
Grid 5	31,530,405	143 h 9 min 20 sec	0.2702	0.0157	0.8194

Table 3.5: Results of grid dependency study

The total transcript time is added to Table 3.5 in order to compare the computational costs. If all these grids had the same computational cost, the finest grid with the best result would be chosen. This time assumes 40 cores are used. For grid 5 more cores were used, but for comparison it is recalculated to if it would be done with 40 cores. It can be seen in this table, and especially when the convergence time is plotted in Figure 3.16, that this grows exponentially. This is as expected in the 3D space where every length is changed with the reference height, and thus the number of nodes also increases exponentially.

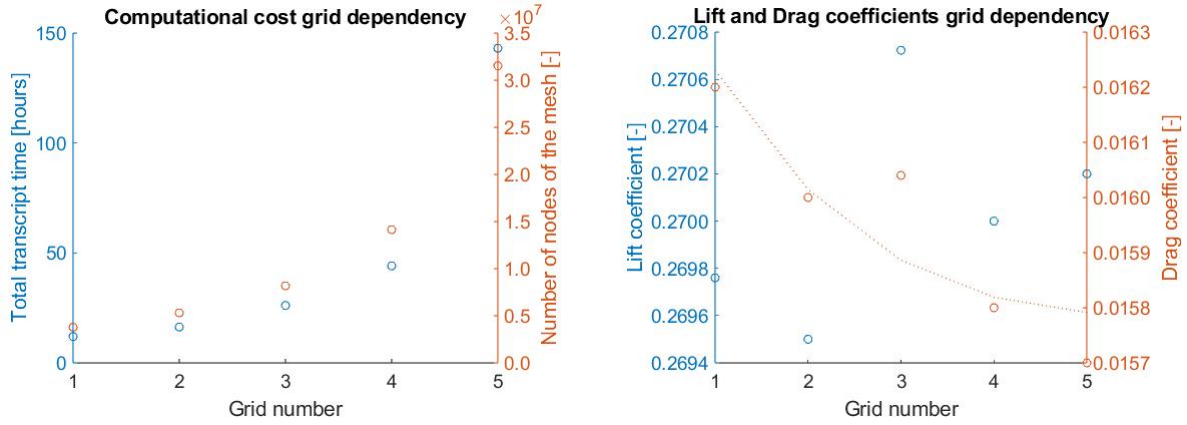

(a) Total transcript time and number of nodes.

(b) Output parameters grid dependency study

Figure 3.16: Grid sizes and output parameters plotted.

Looking at the results in Figure 3.17 it can be seen that the trend is very similar for the different grids used. The lift distribution has a ellipse shape, as expected, that goes down slightly at the root. This is because the lift coefficient is calculated per section, and since the wing has taper, the chord decreases and thus the lift coefficient distribution goes down towards the root. The magnitude of the difference between the grids compared to grid 3, is at most 0.6%, as can be seen in Figure 3.17b.

The drag variation across the span is not smooth, as seen in Figure 3.17c. The drag calculated at each section of the wing has a lot of noise. Again, this is most likely a post-processing error with the sectional drag calculations. Because it seems like a local effect, the general trend is compared, realising that the span distribution should look smoother than this. However, between the different grids, no significant differences in accuracy can be observed. The magnitude of the difference between the grids compared to grid 3, is at most 6%, as seen in Figure 3.17d.

Then, in order to quantify the uncertainty due to the grid discretization, the standard deviation of the lift coefficient and drag coefficient data is found. The data points, as shown in Figure 3.16 look quite scattered for both datasets. For the lift coefficient, the fit is found to be oscillatory, and the standard devaition is based on that. For the drag coefficient, the data points can be fitted better, and this will be further discussed.

Since the data points for the lift coefficient are found to be oscillatory, it is difficult to estimate a solution. Therefore, the standard deviation for each grid is calculated with a 'safety factor' of 3. This ensures the solution is within that error band with 95% confidence based on experience [31]. This means that the final standard deviation is 3 times the difference between the maximum and the minimum data point for that solution. This maximum difference is 0.001, and thus small relative to the lift coefficient value. This leads to a lift coefficient standard deviation, with the safety factor, of 1.32-1.33% for all grids.

When the same approach is applied to the drag coefficient data points, the biggest difference is greater relative to the value of the drag coefficient. These results, as a percentage of the estimated exact solution, are given in Table 3.6. However, it is also noted that this biggest difference is between grid 1 and grid 5, as the trend of the data points is that it is going down, with an exception of grid 3. When these points are fitted with a least-square fit, an estimated solution of 0.0157 is found. The standard deviation with a converging solution , based on the method of Eça and Hoekstra, is between the grid solution and the estimated solution. When using this method, though still using a safety factor of 3, the standard deviation is given in Table 3.7. This is significantly lower than with the maximum difference method. This is especially for the finer grids, which are expected to be more accurate. However, still only 5 data points are used. This make it uncertain if grid 3 is indeed such an outlier, or if the data points can not be fitted well at all. Nevertheless, the high standard deviations as displayed in Table 3.6 are expected to be on the very high end, since grid 4 is chosen and by fitting this will only give a standard

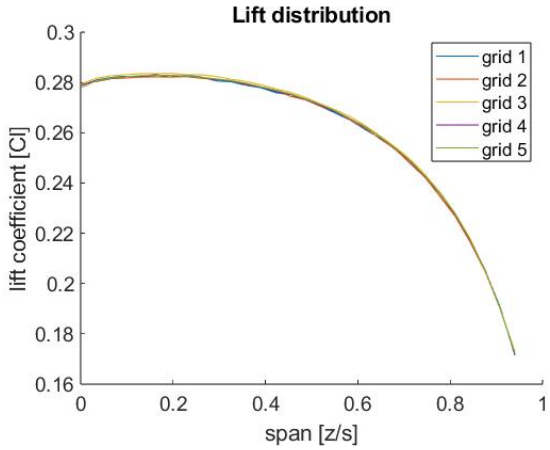

(a) Span lift distribution

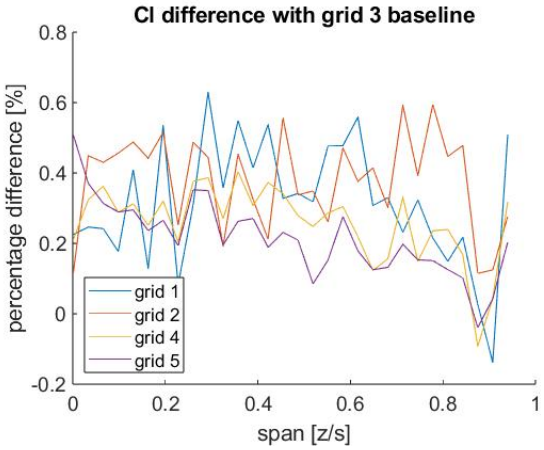

(b) Lift distribution relative difference

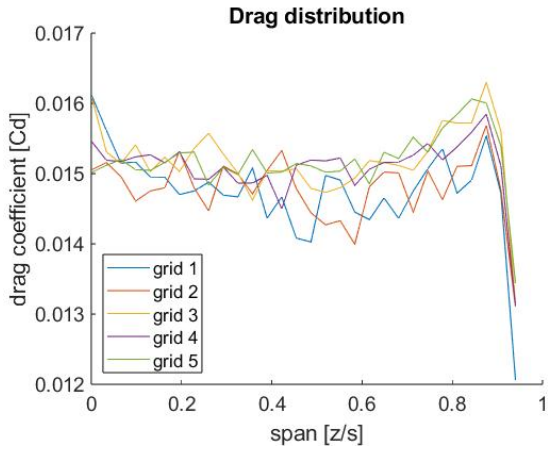

(c) Span drag distribution

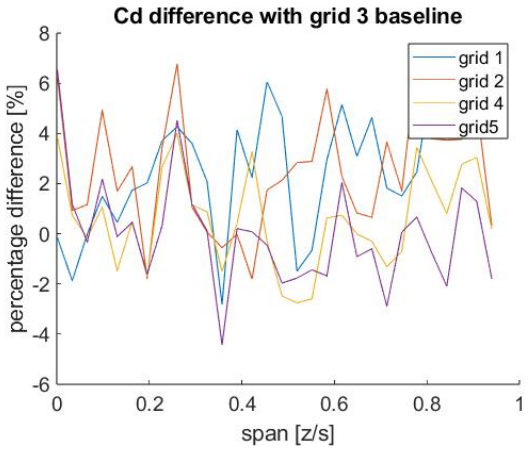

(d) Drag distribution relative difference

Figure 3.17: Grid dependency study results

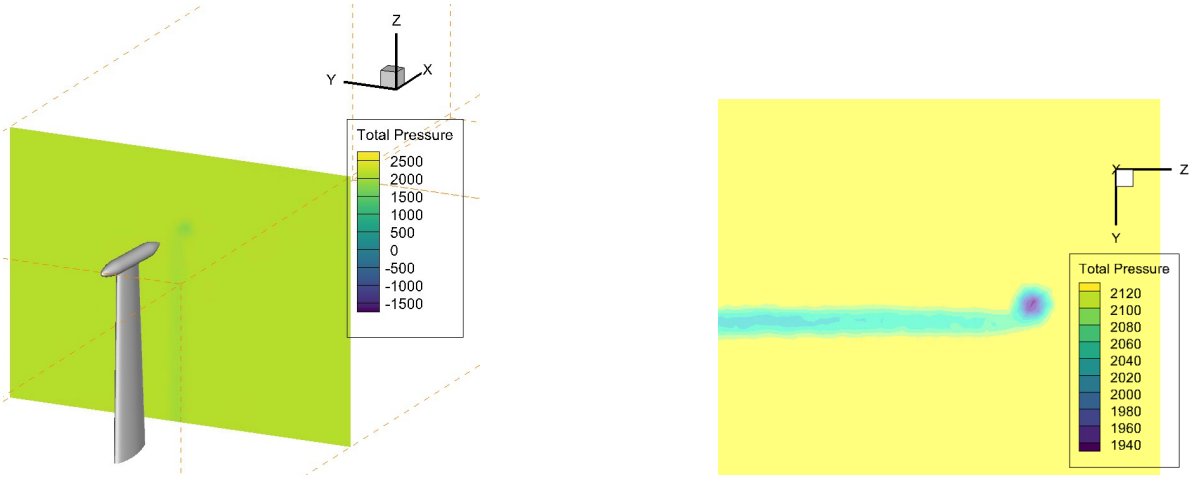

Figure 3.18: Wake screen showing total pressure.

deviation of 0.3%.

For both cases, estimating the standard deviation is done though it can be visually observed that the fit is quite poor. If for example the first two points would be removed, the fitted estimation curve would be very different for both cases. However, it can be concluded that for the lift coefficient the maximum difference already is not a big uncertainty between the grids, and for the drag coefficient the finer grids are closer to the estimated value.

Grid	U_{Cl} [%]	U_{Cd} [%]
1	1.33	9.25
2	1.33	9.38
3	1.32	9.35
4	1.32	9.49
5	1.32	9.55

Table 3.6: Discretization Uncertainty (U) from thrice the maximum difference, as percentage of grid values.

Grid	U_{Cd} [%]
1	7.93
2	4.13
3	4.89
4	0.33
5	1.57

Table 3.7: Discretization Uncertainty (U) from data points and estimated solution, as percentage of grid values.

Lastly, an important phenomenon to look at for the dependency study is the total pressure in the wake. For this research the interest will be on the flow phenomena around the wing tip, so how well this area is modelled is relevant for this study. The location of this total pressure analysis is done at 1.5 MAC behind the trailing edge of the wing, as this is also where future analysis will be done. The pressure can visually be seen in Figure 3.18.

In Figure 3.19 the total pressure at the wing-tip versus the lateral position is shown. Here the difference between the grid fineness is very significant. The finer the grid, the less diffused vortex is. This makes sense as a lower resolution leads to a higher numerical dissipation and diffusion. This also results in the finer grids having a higher peak in pressure drop. The difference between the minimum total pressure in grid 3 and grid 5 is about 12.2%.

To compare the total pressure drop, the results in Figure 3.19 should be integrated.

$$\text{total pressure drop} = \int_{-0.2}^{0.2} (1 - Cp_{tot}) d\left(\frac{y}{s}\right) \tag{3.8}$$

The results are (0.0062, 0.0074, 0.0078, 0.0090, 0.0105) for the wing tip location (grid 1, grid 2, grid 3, grid 4, grid 5) respectively. This means that the error between grid 3 and grid 5 is now 25.7%, but is reduced to 14.3% for between grid 4 and 5. For this reason, grid 4 is chosen to continue with.

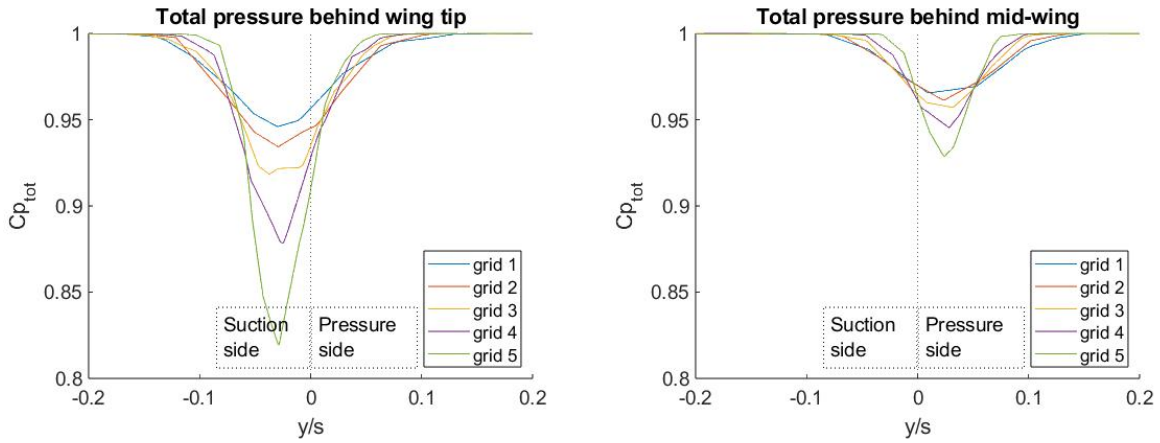

(a) At the wing tip location (z/s = 1.0).

(b) At the mid of the wing (z/s = 0.5).

Figure 3.19: Total pressure coefficient in the wake 2.5 MAC behind wing LE.

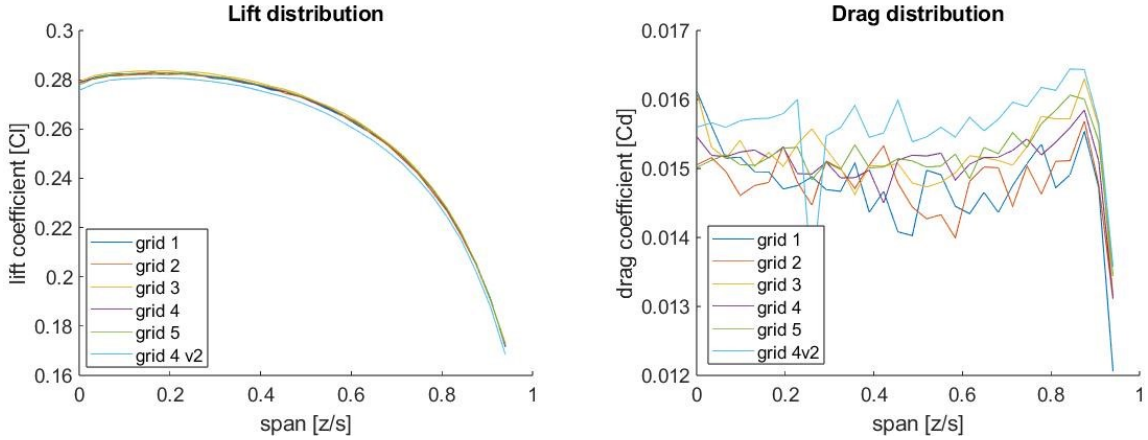

(a) Grid dependency of span lift.

(b) Grid dependency of span drag.

Figure 3.20: Span loading of grid dependency cases, with new adjusted case added.

3.3.3. Adjustments

Like described in subsection 3.2.7, adjustments had to be made to have the cases with propeller installed converge well. This has been done successfully, such that the data processing can be proceeded. However, because the adjustments are done later in the progress, the verification of the mesh is not valid anymore. However, since this second version of grid 4 is available, the grid dependency can be considered reliable if this grid shows the same properties as the first version of grid 4. To check to what extent the new mesh is different from the dependency study done, the results of the grid is plotted in Figure 3.20. As can be seen, the lift distribution values are distanced from the other grids. This makes the whole study incomparable. Because the boundary layer is modelled differently, it can be expected that the lift distribution shifts. Also, it can be noted that qualitatively the results are similar and the percentage change is 0.9 - 1.5% across the span. Unfortunately, a new dependency study should be done to properly analyse this discrepancy. But because the outcome is as expected, the same range of uncertainty is expected from the new dependency study. This is not a problem for the research question investigated in this thesis, as results are compared relative to each other.

4

Results

In this chapter, the results are analysed to quantify the effect of excluding the nacelle in tip-mounted propeller research on the wing performance parameters and other installation effects. Several effects of having the nacelle, with or without the propeller, will be compared to do this. Firstly, the integrated lift and drag coefficients of the wing, and the distribution along the span. And the other installation effects looked at are the total pressure and the swirl angle in the wake of the wing, with the aim of explaining aspects of vortex behavior.

Just as described in the method diagram in Figure 3.2, four main analyses are made: comparing the propeller-off nacelle effect in section 4.1, comparing the propeller-on nacelle effect in section 4.2, comparing the effect of the nacelle on the propeller installation effect in section 4.3, and comparing the isolated actuator disk loading with the installed actuator disk loading. The latter is discussed in Appendix A, where the isolated loading is selected as input loading. Furthermore, in Appendix B pressure fluctuations that are found on the wing and this phenomenon impact on the results are discussed.

4.1. Nacelle effect without propeller

Firstly, the effect of a nacelle is investigated without the propeller installed yet. So from the four configurations discussed in section 3.1, the 'w' (wing only) and 'wn' (wing and nacelle) configurations are compared in this section. These cases used for this investigation are shown in Figure 4.1.

4.1.1. Performance parameters

The lift and drag coefficients and distributions of the wing with and without the nacelle are first investigated. This is done by adding the nacelle, and calculating the integrated lift and drag values along the

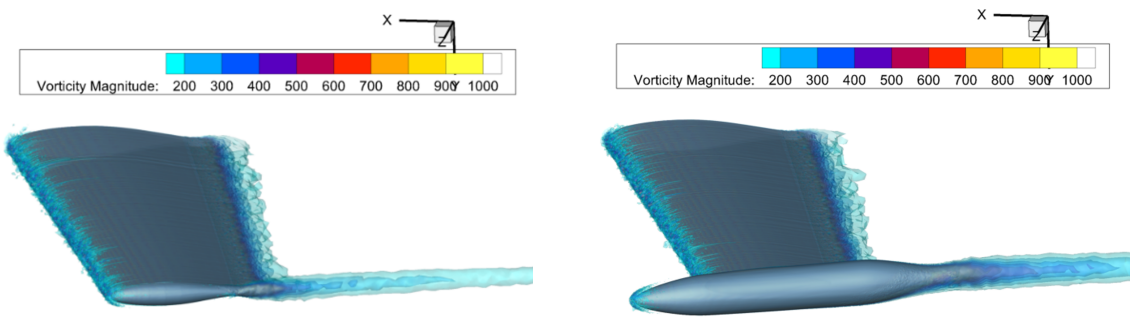

(a) Case 1, 'w': wing only.

(b) Case 2, 'wn': Wing and nacelle.

Figure 4.1: Result visualisation for no-propeller cases.

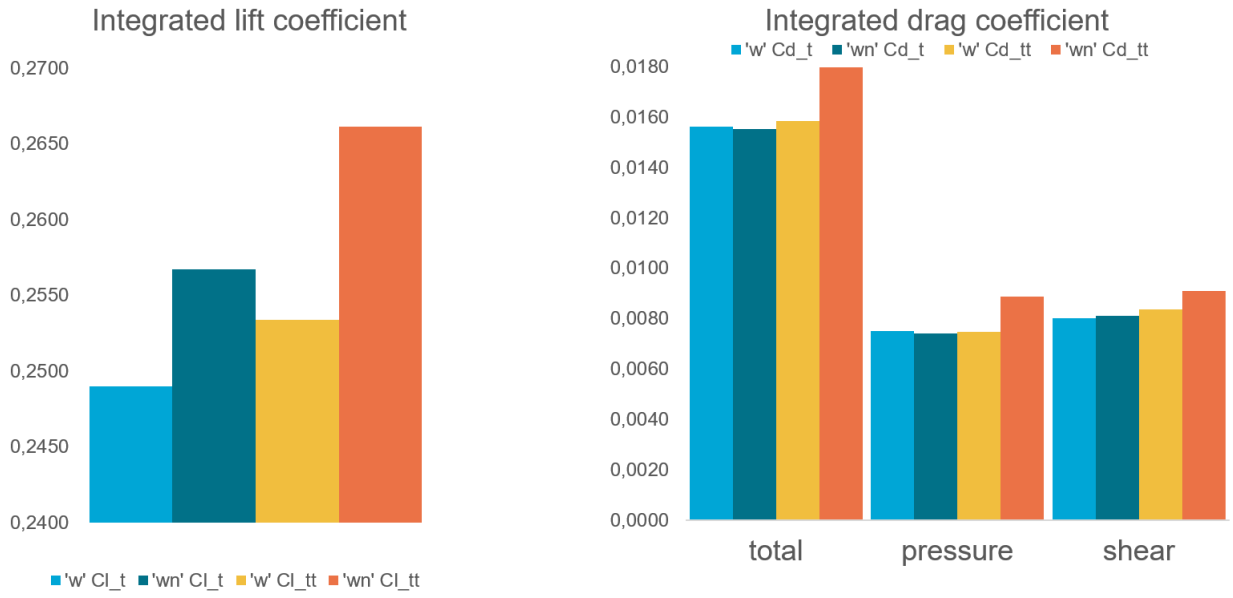

(a) Lift coefficient, without (blue) and with (orange) tip surface.

(b) Drag coefficient, without (blue) and with (orange) tip surface.

Figure 4.2: Performance parameters comparing without ('w' case) and with ('wn' case) nacelle

span of the wing. This integrated coefficient is calculated both without and with the wing tip or nacelle surface included to compare both.

The coefficients can be calculated locally per section, or for the total wing. The local coefficients, Cl_l and Cd_l are used for the span distributions in Figure 4.3. These are calculated with the local chord at each section. Along the wing span, 150 slices are made to calculate the local coefficients. The total coefficients, Cl_t and Cd_t are compared when given the integrated values. These are calculated with the wing planform surface area (S) without wing tip or nacelle. This surface is chosen because the coefficients are then comparable even with the changing geometry of the wing tip or nacelle. Although the span is normalised in the model, the integral is multiplied by the span to get the total lift, then normalised again with the wing planform surface area S. In other words, instead of using the local chord at each section, for the integrated values the mean chord ($\bar{c}$) is used, which is slightly different from the Mean Aerodynamic Chord (MAC) given of this model [32].

To compare the performance parameters, lift and drag of the wing, these are integrated along the span of the wing. For this, first the nacelle in the 'wn' case and the wingtip in the 'w' case are not included, these parameters are labelled Cl_t and Cd_t. Then, also the lift and drag of these tip and nacelle surfaces are included in the comparison, these are labelled Cl_{tt} and Cd_{tt}.

In Figure 4.8a it can be observed that the lift coefficient increases when the nacelle is added in the configuration (from 'w' to 'wn'), and it increases when the nacelle and tip surface is included in the integral (from blue to orange). This means that the lift distribution across the wing increases when the nacelle is added. This is confirmed by looking at the span distribution of the lift in Figure 4.3a.

Without the nacelle and wingtip included, the drag change (ΔCd_t) is very small and thus the overall lift over drag increases by 2.2%. When the nacelle and wingtip are included in the integrated coefficient, this results in a drag increase, because the nacelle leads to shear drag (8.43%) as well as pressure drag (18.92%). This pressure drag is mostly at the nacelle location itself, because it is not seen when just the wing surface is integrated. Overall, this lead to the lift over drag of the wing decreasing by 7.4%.

The same effect is observed with the span distributions of lift and drag. This is shown in Figure 4.3. For the drag distribution, apart form the nacelle location itself the distribution is similar. For the lift distribution, the nacelle leads to an increased lift across the whole span. From this, it can be interpreted that the nacelle presence has the same effect as a wingtip, thus leading to a higher lift. The difference between these cases ranges between 1% at the root and 15% at the tip. This difference in absolute

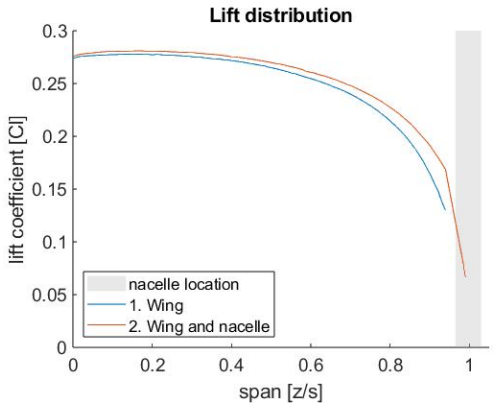

(a) Lift distribution without propeller.

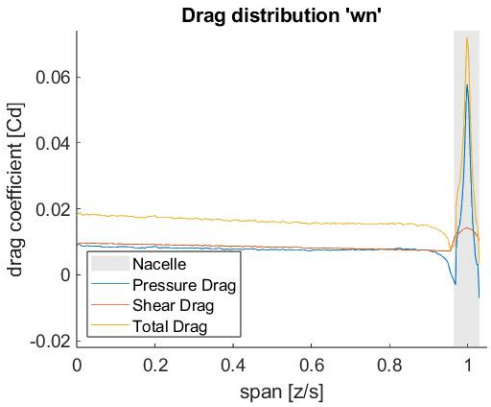

(b) Drag distribution components with nacelle, without propeller.

Figure 4.3: Span distribution of lift and drag showing effect of nacelle.

value is closer to each other, but due to the elliptical shape of a lift distribution the relative difference increases towards the tip.
The drag distribution along the wing span does not change significantly when adding the nacelle. The drag at the nacelle location is high, especially due to the pressure drag. The pressure drag is negative on the sides of the nacelle, as well as on the wing tip for the wing only 'w' case. This effect is most likely a local modelling error, and thus not taken into account. For the wing only 'w' case, the pressure distribution along the chord close to the root shows small pressure fluctuations on the leading edge pressure side. This is further looked into in Appendix B, but has no effect on the overall drag coefficient or distribution trend.

In conclusion without the propeller added in the model yet, the lift and drag are increased when the nacelle is added but the lift over drag ratio decreases. The lift coefficient increase is across the wing span, as the nacelle acts as a wingtip. However, the nacelle also adds drag, both pressure and shear drag. Therefore, the overall lift over drag performance goes down with just the nacelle added.

4.1.2. Installation effects: wake characteristics

Next to the wing performance parameters, other effects from installing the nacelle are discussed. For this analysis, the wake of the wing is investigated. This is done 2.5 Mean Aerodynamic Chords (MAC) behind the leading edge of the wing. This location is chosen between the Particle Image Velocimetry (PIV) plane in experimental simulations was also placed at this location [17]. The aim is to investigate the wake characteristics to analyse vortex behaviour and characteristic parameters change due to the presence of the nacelle.

In this section, the swirl angle in Figure 4.5 and the total pressure behind the wing tip in Figure 4.6 is plotted. These plots are defined such that the center of the plot, coordinate (0,0), is at the wing tip in the middle (y=0). So for cross section a-a', as illustrated in Figure 4.4a, location a is one propeller radius length inboard and a' is one propeller radius length outboard. Therefore, in Figure 4.6a, the positive r/R_p values are outboard and the negative values are inboard. For section b-b', the line is from location b on the suction side to b' on the pressure side, as also illustrated in Figure 4.4a.

In Figure 4.5a it can be observed that adding the nacelle results in a difference in swirl angle, already here without the propeller. The difference illustrates a shift in location, and the maximum angle is increased. The reason that the swirl at this location shifts outboard is likely due to the nacelle physically being there, increasing the span of the wing, and the wing tip vortex forming around the nacelle instead just around the tip. Furthermore, adding the nacelle increases the maximum angle, as seen in Figure 4.5c compared to the case where there is no nacelle as seen in Figure 4.5b. This could be because the pressure differential between the pressure and suction side of the wing is higher (due to the nacelle), as illustrated before in the span distribution in Figure 4.3a.

In Figure 4.6, the total pressure 2.5 MAC behind the wing is plotted. In Figure 4.6a the total pres-

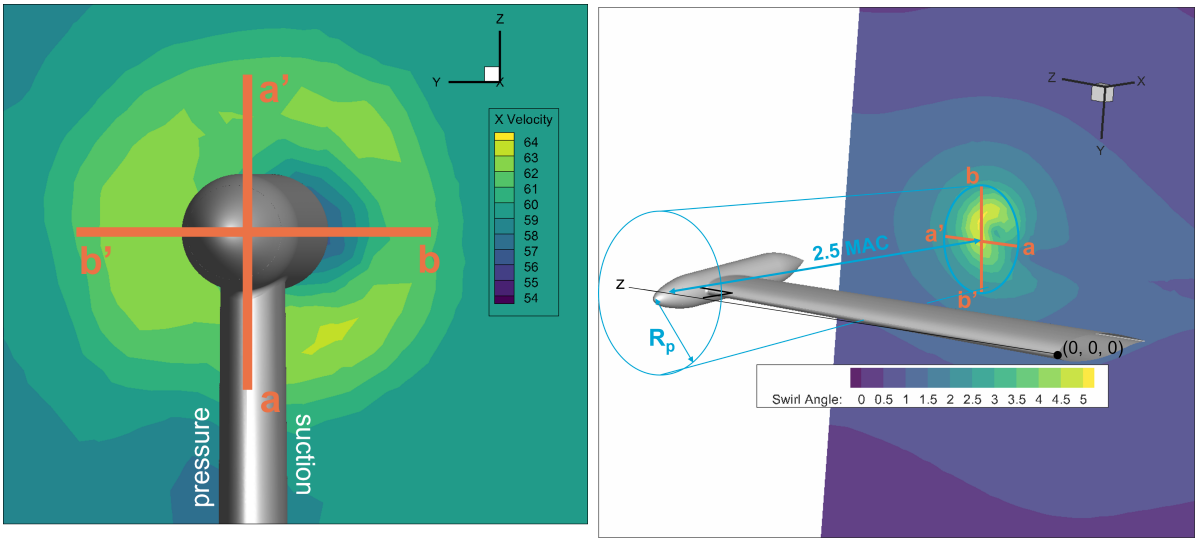

(a) Pressure wake coordinate system.

(b) Visualisation of plane 2.5 MAC behind root LE of the wing.

Figure 4.4: Wake pressure and swirl plane location.

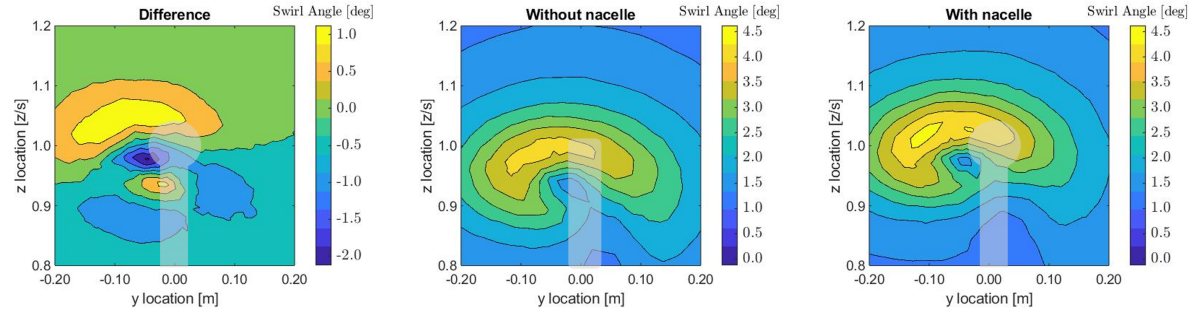

(a) Difference from 'w' to 'wn'.

(b) Swirl angle for case 'w'.

(c) Swirl angle for case 'wn'.

Figure 4.5: Effect of adding nacelle on the swirl angle 2.5MAC behind the LE of the wing.

sure between a and a' is plotted, and in Figure 4.12b the total pressure between b and b' is plotted. In the spanwise distribution of Figure 4.6a the shift of the vortex can also be observed. The location of minimal pressure moves outboard when the nacelle is added. Furthermore, in both plots it can be seen that the total pressure decreases when the nacelle is added, due to the frictional losses.

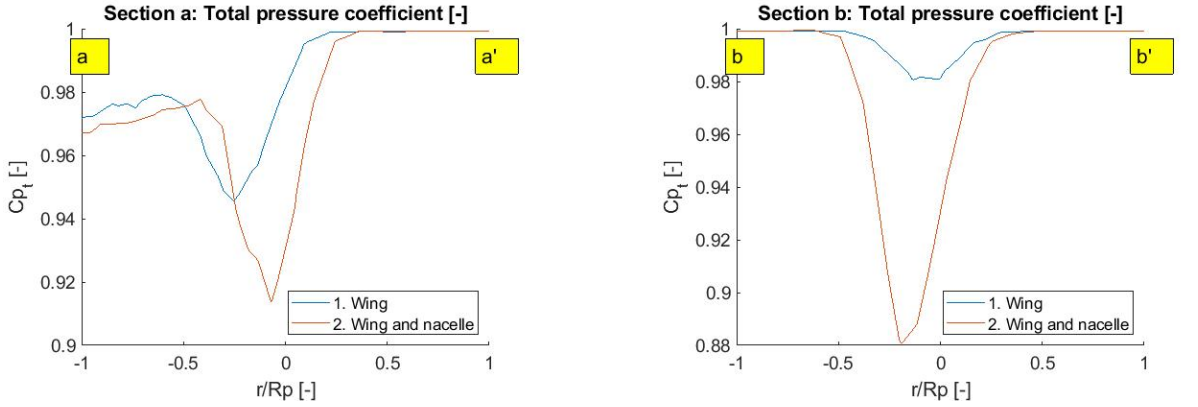

(a) Total pressure coefficient at section a-a' in Figure 4.4a.

(b) Total pressure coefficient at section b-b' in Figure 4.4a.

Figure 4.6: Total pressure in the wake of the wing only 'w' and wing and nacelle 'wn' setup.

To sum up, the wake characteristics of the wing reveal that the presence of the nacelle amplifies the maximum swirl angle as the vortex strengthens. Additionally, the vortex's location shifts due to the nacelle, and there is a more pronounced decrease in total pressure when the nacelle is incorporated. Apart from these observations, the rest of the results bear a strong resemblance to each other, and the identified trends are consistent.

4.2. Nacelle effect with propeller on

Then, the same comparisons are done with the propeller installed. Since the propeller is modelled with an actuator disk model, the input loading of this model is first analysed. This is done in Appendix A. From this data, the installed disk loading is chosen, and the effect of the nacelle is discussed in section 4.2. The chosen loading is the isolated loading, because it is concluded in Appendix A that these flow characteristics are close enough to the installed case, and an isolated propeller loading is more versatile.

The new configurations are shown in Figure 4.7 to give an overview of the results that are compared, in addition to the results in Figure 4.1. Also, a good manner to check that the behaviour is as expected. Quantitatively, there are no conclusions drawn from these images, shown in Figure 4.7. Just that the verification can be done that the disk model is implemented at the right location and orientation, and it is clear what cases are compared and how that flow field looks like.

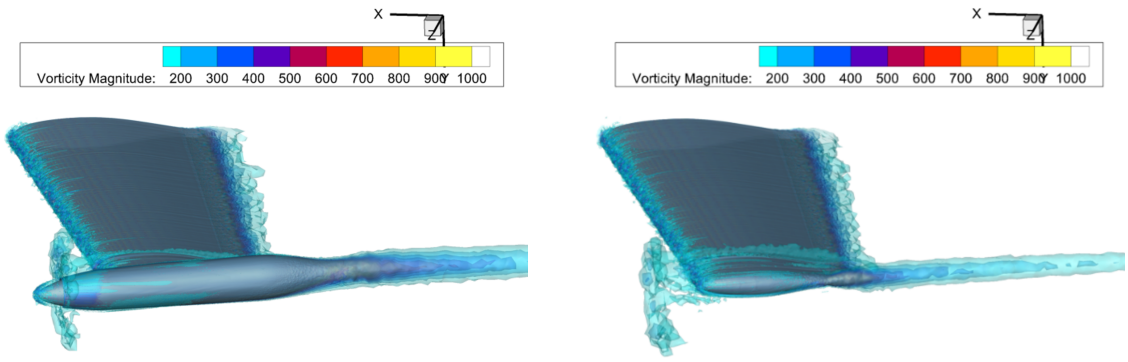

(a) Case 3: Wing, nacelle and propeller.

(b) Case 4: Wing, and propeller.

Figure 4.7: Visualisations of the four cases.

4.2.1. Performance parameters

Then, the overall performance parameters can be looked at to see how the nacelle influences the flow field and thus the overall performance of the wing.

In Table 4.1, the lift, drag and lift over drag (L/D) are shown for each case. In Figure 4.8 it can be seen and compared that the trend with the propeller on are the same as in section 4.1 with the propeller off. Then, in Table 4.3 the effect of removing the nacelle is shown, so going from 'wn' to 'w' and from 'wpn' to 'wp'. This is defined, for example the lift coefficient, as $\Delta Cl = (Cl_w - Cl_{wn})/Cl_{wn}$. In these differences, the differentiation between the planform coefficient and the coefficient including the tip and nacelle is made again. For Cl_t, Cd_t and L/D_t the nacelle is not added to the integration of lift and drag. This way, the same geometry of the wing is compared. The coefficients Cl_{tt}, Cd_{tt} and L/D_{tt} do include the lift and drag on the nacelle and wing tip, because this has an effect on the overall performance.

Also with the propeller installed, it can be seen that removing the nacelle decreases both the drag and lift. This is in case just the wing planform is used, as well as the total coefficient with the tip and nacelle included. The change in drag is negligible when not including the nacelle surface itself, but the nacelle itself adds both pressure and shear drag. This can be clearly seen in Figure 4.8, and results in more than 11% change in Table 4.3. The change in lift coefficient is already higher as discussed in the propeller-off case. With the propeller, the difference in lift is higher than without the propeller. That is, 2.75% without the propeller and 3.18% with the propeller. Because the drag coefficient has such

an increase when the nacelle surface is included, the overall lift over drag goes up when removing the nacelle. The lift over drag performance is lowest for the 'wn' case, as seen in Table 4.5. This clearly portrays that the nacelle itself and the effect on the wing performance is not benefition for the aerodynamic performance. This disadvantage decreases when the propeller is installed, as seen in Table 4.4. However, in these conditions the nacelle always decreases the overall performance, and the nacelle especially adds a lot of local drag.

	'w' case	'wn' case	'wpn' case	'wp' case
Lift coefficient [-]	0.2513	0.2590	0.2666	0.2581
Drag coefficient [-]	0.0157	0.0156	0.0155	0.0155
Pressure drag coefficient [-]	0.0076	0.0075	0.0074	0.0075
Shear drag coefficient [-]	0.0081	0.0082	0.0081	0.0081
L/D [-]	15.96	16.56	17.16	16.61

Table 4.1: Performance parameters of wing planform only.

	'w' case	'wn' case	'wpn' case	'wp' case
Lift coefficient [-]	0.2534	0.2661	0.2784	0.2633
Drag coefficient [-]	0.0158	0.0180	0.0181	0.0159
Pressure drag coefficient [-]	0.0075	0.0089	0.0089	0.0075
Shear drag coefficient [-]	0.0084	0.0091	0.0092	0.0085
L/D [-]	15.99	14.81	15.41	16.51

Table 4.2: Performance parameters including tip and nacelle surface.

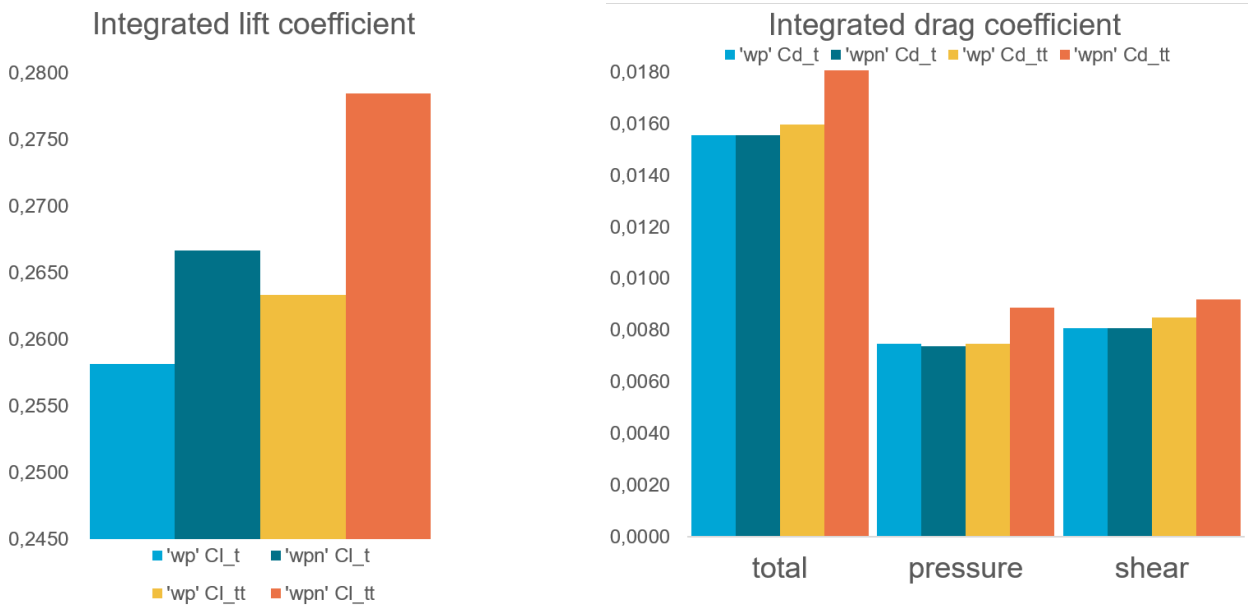

(a) Lift coefficient, without (blue) and with (orange) tip surface.

(b) Drag coefficient, without (blue) and with (orange) tip surface.

Figure 4.8: Performance parameters comparing without ('wp' case) and with ('wpn' case) nacelle

	Without propeller	With propeller
ΔCl_t[%]	-2.75	-3.18
ΔCl_{tt}[%]	-4.78	-5.44

	Without propeller	With propeller
ΔCd_t[%]	-0.65	0
ΔCd_{tt}[%]	-11.80	-11.73

Table 4.3: Effect of removing the nacelle on the lift and drag coefficient.

	Without propeller	With propeller
Difference in L/D of the wing planform [%]	-2.12	-3.2
Difference in L/D including tip and nacelle [%]	7.96	7.13

Table 4.4: Difference in lift over drag performance when removing the nacelle.

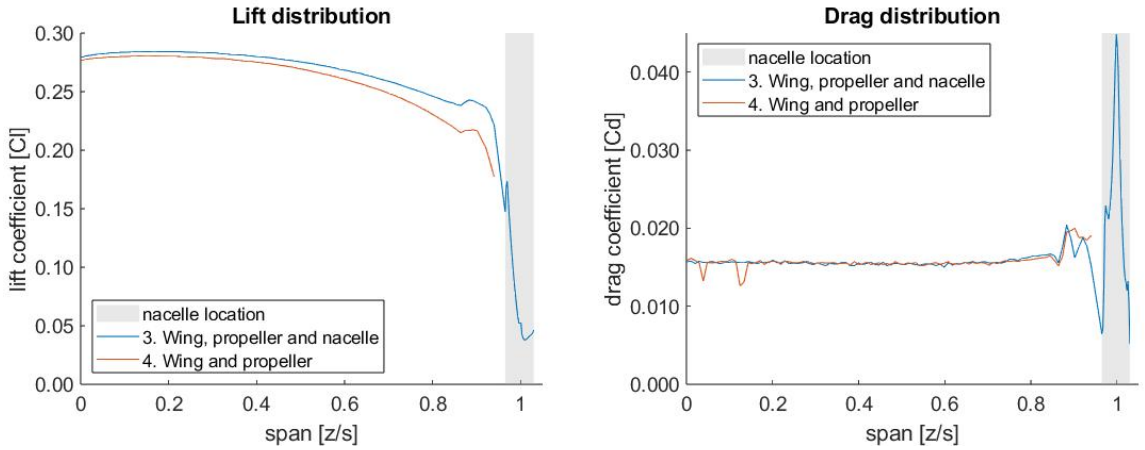

(a) Lift distribution with/without nacelle with propeller.

(b) Drag distribution with/without nacelle with propeller.

Figure 4.9: Span distribution with the propeller installed.

This local drag increase due to the nacelle can also clearly be seen in Figure 4.9a. Across the wing, the drag has a similar distribution, except for the two drops around 0.1s that will be discussed in Appendix B. At the propeller location, the drag increases in both cases, but on the nacelle itself the biggest difference is identified. Furthermore, it is again identified that the lift distribution increases across the whole span due to the nacelle present, as results in the parameters discussed above. The nacelle itself still produces some lift, $(Cl_{tt} - Cl_t$ for the 'wpn' case is 0.0118, this is also seen in Figure 4.9a. But the nacelle itself especially adds relatively much drag, as seen in Figure 4.9b.

In conclusion, adding the nacelle increases the lift along the whole wing span, though the drag increase is at the nacelle location itself. Overall, the lift over drag performance with this effect goes down, also when the propeller is on.

4.2.2. Installation effects: wake characteristics

Next to the performance parameters, it is interesting to look at what phenomena occur and change with and without the nacelle. What are the other installation effects of the tip-mounted propeller? Related to the lift and drag, it is investigated how the swirl of the wake behaves, also the tip vortex without the propeller. This section will also look into the location of the phenomena, such as the shift in wake pressure. Knowing this, with and without the propeller, research without propeller installation can be better interpreted. Furthermore, other effects can be related to the streamlines or local pressure distribution on the with at certain span locations.

First of all, the conclusion from literature is confirmed that the wingtip-mounted propeller attenuates the swirl angle in the wake. When the wake angle for case 2 and case 3 are plotted, it can be seen that the swirl angle in the wake decreases by 1 to 2 °. The difference in angle is shown in Figure 4.10. The swirl of the wing only case and the wing with nacelle case is already plotted in Figure 4.5 and the swirl of the case with propeller and nacelle is already plotted in Figure A.5.

Then, the effect of removing the nacelle is investigated. In Figure 4.11 the effect of removing the nacelle is plotted, in the case with the disk model implemented. Also in this case it can be observed that the swirl angle is increased overall on the inboard side, and decreased next to the wing tip. Without the propeller, there is another center on the wing span around 90-95% where the swirl angle is decreased. This effect can be explained by the positioning of the nacelle. Because the nacelle is located between 0.965 and 1.03 x/s, the tip vortex with the nacelle present has to go around the nacelle. When the

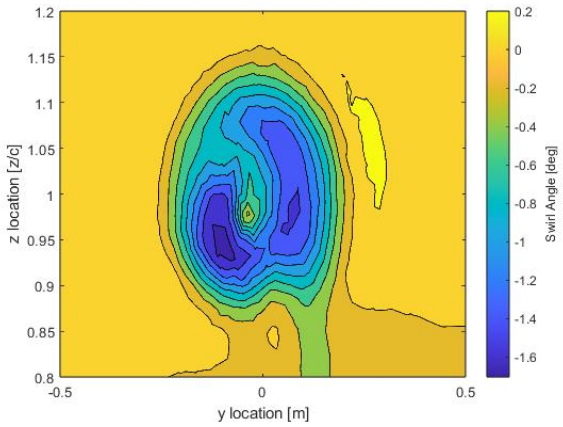

Figure 4.10: Difference adding the propeller (with nacelle).

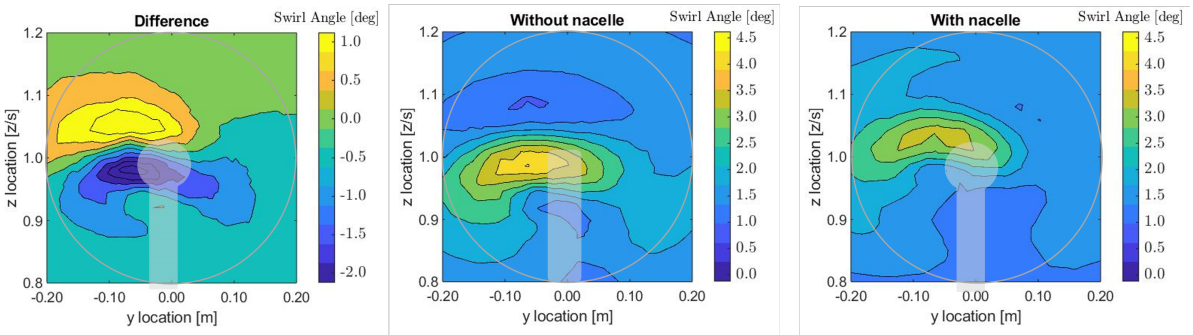

Figure 4.11: Effect of adding nacelle on the swirl angle 2.5MAC behind the LE of the wing.

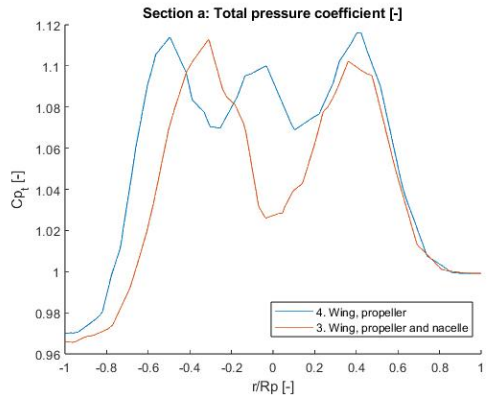

(a) Total pressure coefficient at section a. in Figure 4.4a.

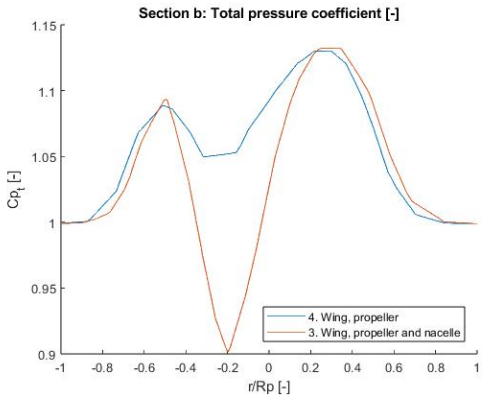

(b) Total pressure coefficient at section b. in Figure 4.4a.

Figure 4.12: Total pressure in the wake with propeller of the wing 'wp' and nacelle 'wpn' setup.

nacelle is removed, the tip vortex is expected to be smaller. This can be observed in Figure 4.7 as well, as the wake diameter is bigger for case 2 and case 3 than case 1 and case 4. So the swirl angle increases inboard and decreases outboard also because the vortex moves inboard.

Finally, the total pressure at the plane behind the wing is compared. This is still the same plane as illustrated in Figure 4.4. To save space, only the total pressure coefficient is shown in Figure 4.12, as the axial velocity looks similar. Also in these graphs, it can be observed that without the nacelle the wake moves inboard. The same explanation applies, where the geometry influences the locations of the tip vortex. Additionally, the total pressure decrease in the wake is much bigger when the nacelle is added.

These effects can be seen both in Figure 4.6a and 4.12a. In addition, it can be seen here that next to the expected increase in total pressure for both cases with the propeller, the total pressure in the middle of the vortex also increases for case 4. This is the effect of the middle of the disk model not having distributions. A gap is present where otherwise the nacelle would be present. It can be observed that this leads to an increase in total pressure and axial velocity in the wake.

4.3. Effect of tip-mounted propellers with and without nacelle

In this section, the effect of the nacelle on the tip-mounted propeller research is investigated. In other words, how are the results of adding a propeller influenced by the presence of a nacelle? This section is relevant for quantifying the effect of excluding or altering the nacelle when doing research on tip-mounted propeller configurations. The effect of adding a tip-mounted propeller, from literature, is that the propeller may increase the drag and lift performance of the wing and it attenuates the swirl angle in the wake [17]. Now this section is going to investigate to what extent these effects change when the nacelle is present or not.

4.3.1. Performance parameters when adding the propeller

For this section, the change in lift, drag and lift over drag when adding the propeller are compared. For this comparison, only the integrated coefficients including the tip and nacelle are used. These coefficients can be found in Table 4.2 in section 4.2. The change in lift coefficient confirms that adding a tip-mounted propeller increases lift. Also it can be concluded that this effect is bigger with the nacelle installed. This means that when doing research without the nacelle installed, it underestimates the effect of increasing lift.

The drag coefficient also increases slightly when the propeller is installed. However, in absolute terms, this may be an rounding uncertainty in this research. Nevertheless, the overall lift over drag also increases with a tip-mounted propeller installed. Again, this increase is higher when the nacelle is present, and thus researching without nacelle would underestimate this effect.

Underestimating the effect is a good thing in conclusion of this research. It means that the effects found are valid, and in reality may increase.

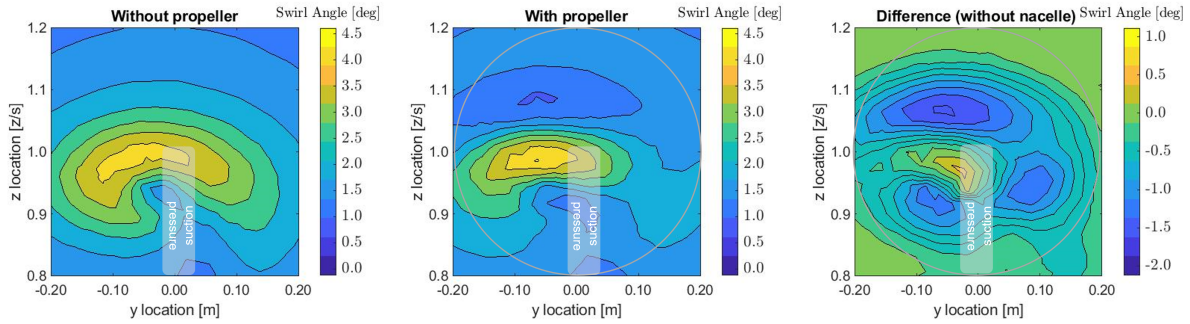

Figure 4.13: Effect of adding propeller on the swirl angle 2.5MAC behind the LE of the wing, without nacelle.

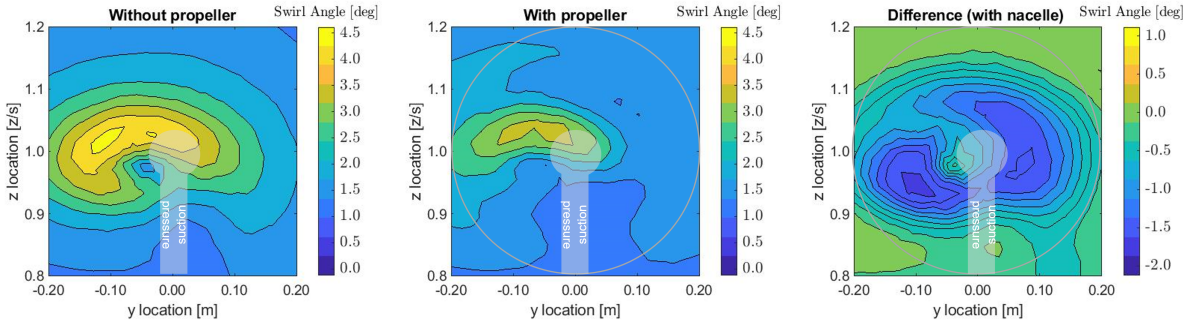

Figure 4.14: Effect of adding propeller on the swirl angle 2.5MAC behind the LE of the wing, with nacelle.

	Without nacelle	With nacelle
ΔCl_{tt} [%]	3.90 %	4.63 %
ΔCd_{tt} [%]	0.64%	0.56 %
L/D_{tt} [%]	3.25%	4.04 %

Table 4.5: Effect of nacelle on tip-mounted propeller performance, including nacelle and tip.

4.3.2. Wake characteristics of adding the propeller

Lastly, the wake swirl characteristics are discussed to compare the differences of adding the propeller with and without the nacelle present.

In both Figure 4.13 (without nacelle) and Figure 4.14 (with nacelle) adding the propeller attenuates the wake swirl angle. This correspondents to the literature on experimental research done before [17]. Furthermore, it looks like the propeller increased the swirl angle in a smaller area on the pressure side of the wing tip. the vortex radius. The vortex core intensified when adding the propeller, though that effect is not present anymore with the nacelle installed.

Comparing the difference in Figure 4.13 with the difference in Figure 4.14, it can be observed that the difference overall is higher when the nacelle is installed. This means again that without the nacelle the effect of the swirl angle is underestimated, though the same trend is observed.

5

Conclusion

In conclusion, the effect of excluding the nacelle in tip-mounted propeller research can be modelled with Computational Fluid Dynamics (CFD) to quantify this effect on the wing performance and flow measurements. For this, the performance parameters of the wing in terms of lift and drag are analysed. Also, swirl angle and total pressure in the wake is investigated to understand the vortex behaviour. This is all done for a configuration set without a propeller, and also with a propeller installed in the form of a disk model. For this disk model, the loading is selected as well.

First of all, the performance parameters analysed change when the nacelle is added. For both the configurations with and without the propeller, the lift over drag increases when the nacelle is removed. The presence of the nacelle leads to a higher lift distribution across the whole span, with an integrated change in lift coefficient of 4.8%. This effect is higher with the propeller present, namely 5.4%. Also, the nacelle presence is the cause of a drag increase at the nacelle location itself, leading to a total drag coefficient increase of 11.8% without the propeller and 11.7% with the propeller installed. Overall, the lift over drag is thus increased when the nacelle is removed, this effect in these configurations is 7 to 8%. So the configuration without nacelle is performing better overall, because both the lift and drag increase due to the nacelle is missing.

Furthermore, the wake characteristics are affected by the presence of the nacelle. Two clear effects are observed: the vortex without the nacelle is more inboard, and the nacelle causes a pressure drop in the wake. The location of the wake swirl shifts inboard when the nacelle is included. This effect is shown with and without the propeller. This is due to the nacelle effect on the tip vortex. Visualizations confirm that the tip-mounted nacelle affects the flow field, and the maximum swirl angle is higher with the nacelle. Also, the absence of loading in the core of the disk model can be clearly observed in the wake. So removing the nacelle will mainly shift the wake more outboard, and neglect the total pressure loss in the wake.

Also, it is noted that the isolated loading is chosen because the total drag and lift increase is negligible and the pressure distributions are very similar. In conclusion, the trend is the same, but the peaks are higher or lower for the installed case. The total difference in total pressure in the wake is 0.1%, while the peaks have a 1.9% difference. Simultaneously, the effect in swirl angle is 0.35%. It is understandable that these differences present between the two loading cases, but is not expected that the flow field characteristics change sufficiently to deep the installed loading unreliable. The changes are directly related to the loading distribution, which is also explained by theory. This is desirable, because for future research if the location of the disk model would be moved around the installed loading would not be representable. Therefore, the isolated propeller loading is used for the further research.

Finally, the effect of adding the propeller is modelled, with and without nacelle. This concludes to what extent the presence of the nacelle is needed for this research. It is found that the effect on the performance parameters, as well as the effect on the wake swirl is higher with the nacelle installed. So

without the nacelle, the effects are underestimated.

Overall, these findings underscore the importance of considering the installation effects of tip-mounted nacelles on wing aerodynamics, with implications for wing performance and wake characteristics. When research is done on the spanwise or vertical position of the propeller, the effect of the nacelle needs to be accounted for because of the magnitude and the location of the flow properties.

The nacelle has a significant effect on the performance of the wing, and the flow field characteristics. The lift is increased across the wing, the nacelle itself adds drag, the vortex shifts, and the total pressure in the wake changes. It is good to be aware of the changes as described above that the nacelle will entail. However, when investigating the effect of tip-mounted propellers, the same result trends are found though without the nacelle the values at most are conservative. Therefore, with the implications of this decision in mind, it can be argued that moving the nacelle upstream is a justifiable assumption.

6

Recommendations

While researching tip-mounted propellers, more aspects are relevant than those discussed in this thesis. Furthermore, on the topic of CFD validation of the nacelle installation effects, recommendations can be made as well.

To begin with, there are several recommended setup enhancements. Utilizing refined mesh techniques, particularly in the wake region, can improve accuracy. For this, a computer where iterating is more easily done would be required. Another improvement would be to implement hexahedron and polyhedron cells. Previous studies have shown that 3 [33] to 4 [34] times fewer polyhedral cells are needed for comparable accuracy, potentially reducing computational costs. Lastly, conducting the grid dependency studies after propeller installation is advisable to ensure computational accuracy, especially if experience with propeller modeling is limited. Fortunately, this problem did not arise in this research, but this preemptive measure can help mitigate unexpected discretization errors.

Then, for now more work is required on this topic especially for the dependency study and the leading edge pulsations. With the new mesh, the dependency study should be redone in order to draw conclusions on the sensitivity to the grid fineness for the new grid that the conclusions are based on. Furthermore, investigating and addressing pressure pulsations at the leading edge of the wing, particularly in cases without the nacelle, is essential for understanding and mitigating potential flow instabilities.

Furthermore, this research is done as a foundation for subsequent research. Primarily, the streamwise and vertical placement of the propeller. From the literature study it is concluded that it would be interesting to move the propeller upstream, and next to that vary the vertical position of the propeller. If the propeller is moved upstream, it is advised to do this with the nacelle, such that there is no gap in the disk model. Investigating the impact of varying the vertical position of the propeller and nacelle assembly relative to the wing surface can provide insights into optimizing aerodynamic efficiency and reducing interference effects. Doing this research without a propeller at all would be a good first step, before looking at the structural integration. Knowing what the installation effects of the nacelle is, will allow this research to be done with more awareness. Alongside this, experimental validation should be done for these computational findings and research in the future. For now, these results were missing, but it would be relevant to validate the model as well as identify the discrepancy. This is crucial for robustness and reliability in real-world applications.

Lastly, in explore tip-mounted propellers and its design optimisation, it's essential to consider additional aspects beyond those addressed in this thesis. Two such areas are tip strikes and aeroelastic effects. Understanding the potential for tip strike events, where the propeller blades come into contact with nearby structures or surfaces, is crucial for safety and performance considerations. Especially with banking angles, the danger of the propeller is bigger if mounted to the tip than mounted mid-wing. Furthermore, the aerodynamics of the propeller installation is just one area of investigation for the performance. Investigating the aeroelastic behavior of the wing and nacelle assembly, including dynamic interactions and structural responses, is essential for the safety and performance of the aircraft overall.

References

[1] International Civil Aviation Organization. *CORSIA: Carbon Offsetting and Reduction Scheme for International Aviation - 2023 Edition*. Accessed: 2024-05-24. 2023. URL: https://www.icao.int/environmental-protection/CORSIA/Documents/CORSIA%20Brochure/2023%20Edition/CORSIA-Brochure2023-EN-WEB.pdf.

[2] E. van der Sman. *Towards a sustainable air transport system*. Tech. rep. 2021.

[3] M. Minervino, G. Andreutti, L. Russo, and R. Tognaccini. "Drag Reduction by Wingtip-Mounted Propellers in Distributed Propulsion Configurations". In: *Fluids* 7.7 (July 2022). ISSN: 23115521. DOI: 10.3390/fluids7070212.

[4] J. Heeg, B. K. Stanford, A. Kreshock, J. Shen, C. B. Hoover, and R. Truax. *Whirl flutter and the development of the NASA X-57 Maxwell*. Tech. rep. Savannah: International Forum on Aeroelasaticity and Structural Dynamics, June 2019.

[5] Robert G. McSwain, Louis J. Glaab, and Colin R. Theodore. *Greased lightning (GL-10) Performance Flight Research*. Nov. 2017. URL: https://ntrs.nasa.gov/api/citations/20180000765/downloads/20180000765.pdf.

[6] Tristan Kennedy. *We Could All Be Flying in Electric Planes Sooner Than You Think*. Feb. 2020. URL: https://www.vice.com/en/article/m7q7qn/electric-planes-future-aviation-environment.

[7] T. Sinnige and B. Della Corte. *WP5: Technology Validation amp; Roadmap*. May 2022.

[8] T. K. Lindner, J. Oldeweme, P. Scholz, and J. Friedrichs. "Experimental Propeller Placement Analysis for a Distributed Propulsion Wing Section in High Lift Configuration". In: American Institute of Aeronautics and Astronautics (AIAA), June 2023. DOI: 10.2514/6.2023-3539.

[9] L. L. M. Veldhuis. *Propeller Wing Aerodynamic Interference Sustainable Aviation View project Boundary layer instabilities over a rotating body of revolution View project*. Tech. rep. 2014. URL: https://www.researchgate.net/publication/27341924.

[10] J. D. Anderson. *Computational Fluid Dynamics: The basics with applications*. McGraw-Hill, 2010.

[11] M. Felli. "Underlying mechanisms of propeller wake interaction with a wing". In: *Journal of Fluid Mechanics* (2020). ISSN: 14697645. DOI: 10.1017/jfm.2020.792.

[12] L. L. M. Veldhuis. "Propeller Wing aerodynamic interference (thesis)". In: (2005).

[13] E. W.M. Roosenboom, A. Stürmer, and A. Schröder. "Advanced experimental and numerical validation and analysis of propeller slipstream flows". In: *Journal of Aircraft*. Vol. 47. 1. American Institute of Aeronautics and Astronautics Inc., 2010, pp. 284–291. DOI: 10.2514/1.45961.

[14] N. Van Arnhem, T. Sinnige, T. C.A. Stokkermans, G. Eitelberg, and L. L. M. Veldhuis. "Aerodynamic interaction effects of tip-mounted propellers installed on the horizontal tailplane". In: *AIAA Aerospace Sciences Meeting, 2018*. Vol. 0. 210059. American Institute of Aeronautics and Astronautics Inc, AIAA, 2018. ISBN: 9781624105241. DOI: 10.2514/6.2018-2052.

[15] T. C. A. Stokkermans. *Design and Analysis of Swirl Recovery Vanes for an Isolated and a Wing Mounted Tractor Propeller*. Tech. rep. URL: http://repository.tudelft.nl/..

[16] M. H. Snyder. *Effects of a wingtip-mounted propeller on wing lift, induced drag, and shed vortex pattern*. Tech. rep. May 1967. DOI: 10.2514/3.44076.

[17] T. Sinnige, N. Van Arnhem, T. C. A. Stokkermans, G. Eitelberg, and L. L. M. Veldhuis. "Wingtip-mounted propellers: Aerodynamic analysis of interaction effects and comparison with conventional layout". In: *Journal of Aircraft* 56.1 (2019), pp. 295–312. ISSN: 15333868. DOI: 10.2514/1.C034978.

[18] S. Taniguchi and A. Oyama. “Numerical Analysis of Propeller Mounting Position Effects on Aerodynamic Propeller/Wing Interaction”. In: *AIAA Science and Technology Forum and Exposition, AIAA SciTech Forum 2022*. American Institute of Aeronautics and Astronautics Inc, AIAA, 2022. ISBN: 9781624106316. DOI: 10.2514/6.2022-0153.

[19] R. Felix de Souza and P. A. G. Ciloni. *Aerodynamical Influence of Propeller Lateral and Vertical Position on Wing Induced Drag*. Tech. rep. July 2021. DOI: 10.2514/6.2021-2533.

[20] R. R. Duivenvoorden, N. Suard, T. Sinnige, and L. L .M. Veldhuis. “Experimental Investigation of Aerodynamic Interactions of a Wing with Deployed Fowler Flap under Influence of a Propeller Slipstream”. In: *AIAA AVIATION 2022 Forum*. American Institute of Aeronautics and Astronautics Inc, AIAA, 2022. ISBN: 9781624106354. DOI: 10.2514/6.2022-3216.

[21] J. D. Anderson. *Fundamentals of aerodynamics*. Mcgraw-hill Publishing Co., 2007.

[22] T. C. A. Stokkermans, N. Van Arnhem, T. Sinnige, and L. L. M. Veldhuis. “Validation and comparison of RANS propeller modeling methods for tip-mounted applications”. In: *AIAA Aerospace Sciences Meeting, 2018*. Vol. 0. 210059. American Institute of Aeronautics and Astronautics Inc, AIAA, 2018. ISBN: 9781624105241. DOI: 10.2514/6.2018-0542.

[23] F. Götten, M. Marino, and C. Bil. *A review of guidelines and best practices for subsonic aerodynamic simulations using RANS CFD*. 2019. ISBN: 9781925627404. URL: https://www.researchgate.net/publication/337756101.

[24] T. Sinnige, J. Goyal, R. Nederlof, and et al. *Future propulsion and integration: towards a hybrid-electric 50-seat regional aircraft (Deliverable D3.3)*. Tech. rep. Grant Agreement Number: 875551. Submitted on 02-01-2023. European Commission, 2023.

[25] German-Dutch Wind Tunnels. *Low-Speed Tunnel*. Accessed: 2024-04-23. 2024. URL: https://www.dnw.aero/wind-tunnels/lst/.

[26] T. Sinnige and B. Della Corete. “Aerodynamic performance of a tip-mounted propeller-wing system at positive and negative thrust”. In: *AIAA AVIATION* (2024).

[27] *Y plus wall distance estimation*. June 2011. URL: https://www.cfd-online.com/Wiki/Y_plus_wall_distance_estimation.

[28] *ANSYS Meshing User’s Guide 13.0*. Nov. 2010.

[29] P. R. Spalart and C. L. Rumsey. *Effective Inflow Conditions for Turbulence Models in Aerodynamic Calculations*. Tech. rep.

[30] *Ansys Fluent 12.0 user’s Guide*. Jan. 2009. URL: https://www.afs.enea.it/project/neptunius/docs/fluent/html/ug/node789.htm.

[31] L. Eça and M. Hoekstra. *Discretization Uncertainty Estimation based on a Least Squares version of the Grid Convergence Index*. Tech. rep. 2006.

[32] B Della Corte, L L M † Veldhuis, and T Sinnige. *Experimental Aerodynamic Investigation of a Wing with a Tip-mounted Tractor Propeller at Positive and Negative Thrust*. Tech. rep.

[33] M. Perić and A. G. Ferguson. “The advantage of polyhedral meshes”. In: 2005.

[34] M. Sosnowski, J. Krzywanski, and R. Gnatowska. “Polyhedral meshing as an innovative approach to computational domain discretization of a cyclone in a fluidized bed CLC unit”. In: *E3S Web of Conferences* 14 (2017), p. 01027. DOI: 10.1051/e3sconf/20171401027.

A

Disk model loading

To move the propeller around using a disk model, the loading should be without the effect of the wing on the propeller. It is possible to simulate the effect of the wing on the propeller for each position, but since this loading then has to be obtained as well, it would be more efficient to simulate the whole propeller instead of using a disk. Since using a disk is much faster, it would be beneficial if the isolated propeller loading can be used. In order to find out how much effect this has, a set-up with wing, nacelle and propeller is used to compare two loading cases: installed propeller data called 'InstalledProp Loading', and isolated propeller data called 'IsolatedProp Loading'.

The loading as input is already discussed in Figure 3.6. Here, the effects of using these two cases on the results are discussed. First of all, the wing loading across the whole wing is similar, just locally around the wing tip the loading is different. This can be seen in Figure A.1, where the loading on the outer part of the wing is plotted. Here it can be observed that inboard of the nacelle, the lift is slightly higher for the isolated propeller input data. On the other hand, the drag is higher for the installed loading, but this is barely visible. In terms of integrated coefficients, the total drag coefficient stays the same, and the total lift coefficient increases with 0.14% from installed to isolated loading. This is considered negligable. The isolated data has a higher loading across the wing, while the installed data is mainly under the wing, this could explain the higher lift.

In Figure A.2 the drag distribution of the isolated propeller data, is plotted separately. For the calculation of this drag coefficient, the Mean Aerodynamic Chord (MAC) is used. This is chosen because the coefficient is inversely proportional to the chord length, which would lead to a distorted result that is hard to interpret. It can be seen that the pressure drag is slightly negative on the sides of the nacelle. This means that at the intersection of the nacelle and the wing, the pressure has a forward component, cause by separation or the vortex, this is visualised in Figure A.3. Furthermore, it is shown in this split of drag components that inboard of the nacelle the bump in drag has a pressure and a shear component. This is because of the increased velocity the pressure coefficient goes up, and the local wing has a higher velocity profile, which increases the shear drag. On the nacelle itself, the pressure drag peaks. The drag split distribution is similar for the first loading, and gives insight in the behaviour around the nacelle.

Then, the development behind the wing for the two loading cases is shown in Figure A.4. These plots reflect the differences in loading as already discussed in Figure 3.6. In the a section, so spanwise, the axial velocity and total pressure of installed loading is higher outboard and lower inboard compared to isolated loading. The differences between the peaks are about a percent of the fraction at both locations, meaning the local difference in axial velocity for example is 0.6 m/s. For section b, higher velocity is expected inboard for the installed loading due to to the presence of the wing and thus effect of circulation and blocking on the original loading. This can be seen in the figure. Furthermore, it is evident that the loading below the wing is higher than above the wing. This would be caused by the angle of the nacelle and propeller, where the wake of the nacelle moves to the suction side compared to the coordinate center of these graphs. This can also visually be seen in Figure 3.7. Since both cases

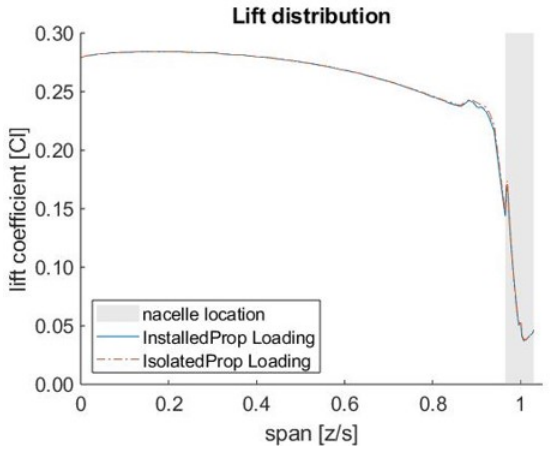

(a) Span lift distribution.

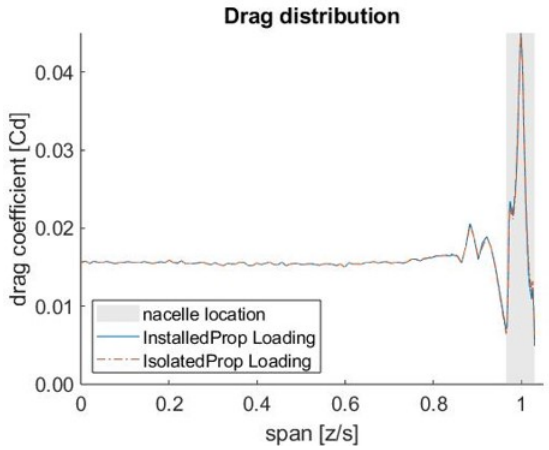

(b) Span drag distribution.

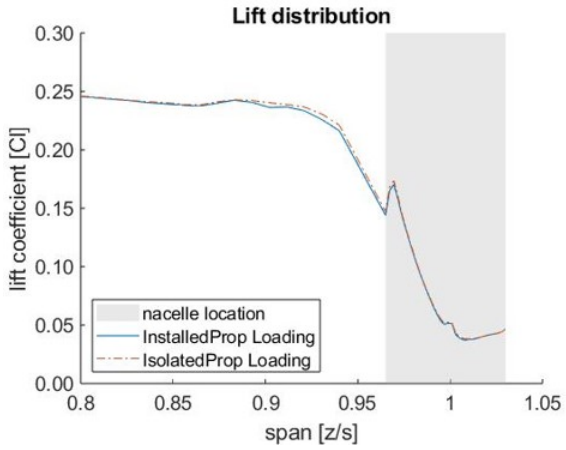

(c) Span lift distribution around the nacelle.

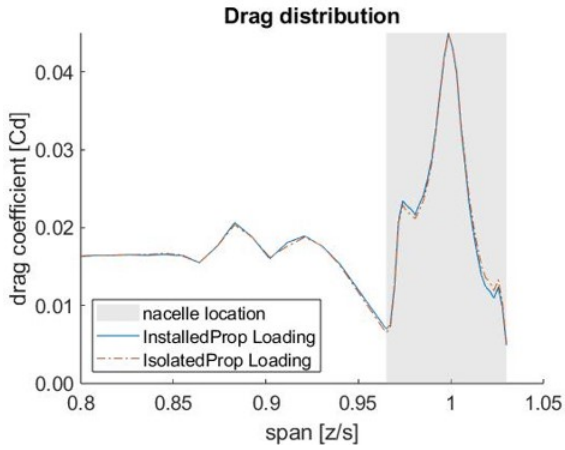

(d) Span drag distribution around the nacelle.

Figure A.1: Span distribution around the nacelle

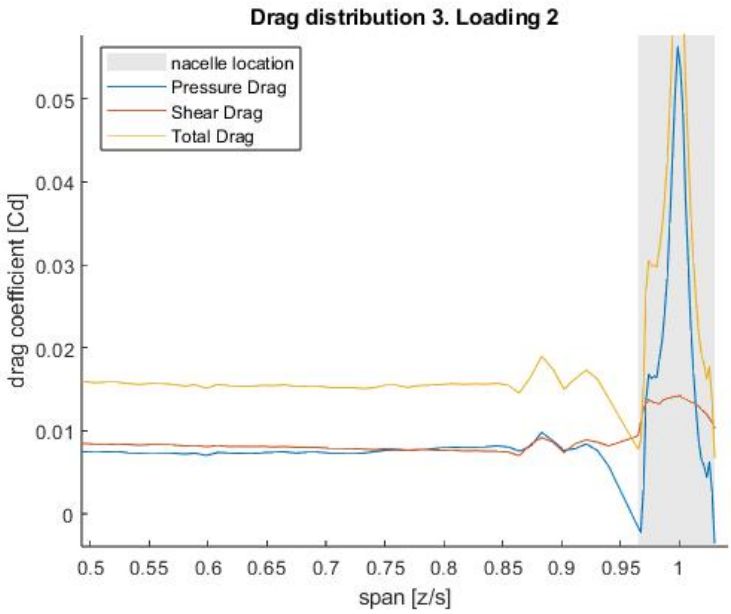

Figure A.2: Drag coefficient split into shear and pressure drag for case 3 with loading 2.

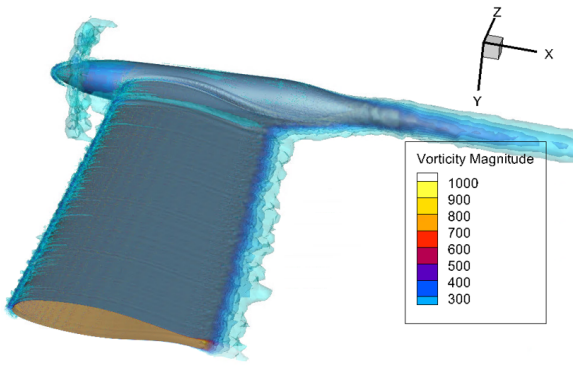

Figure A.3: Visualisation of case corresponding to Figure A.2.

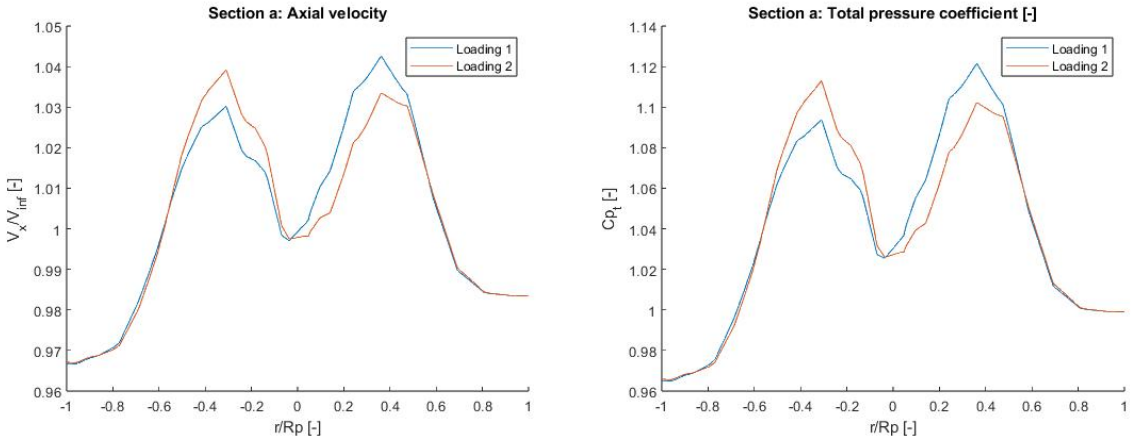

(a) Axial velocity spanwise distribution.

(b) Total pressure spanwise distribution.

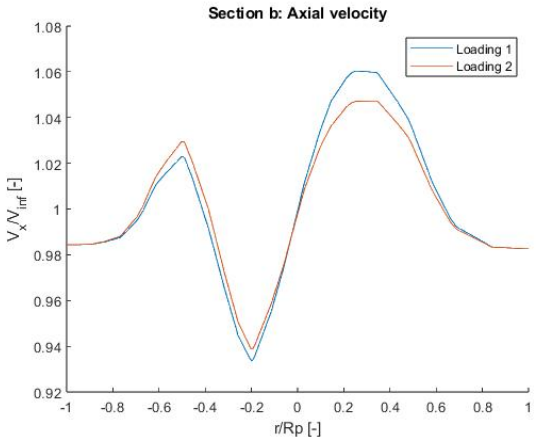

(c) Axial velocity vertical distribution.

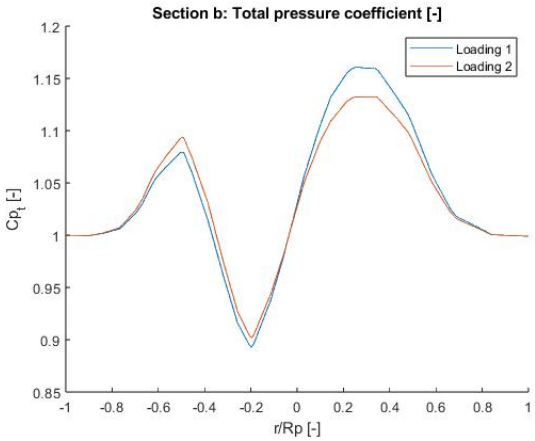

(d) Total pressure vertical distribution.

Figure A.4: Wake pressure graphs at plane 1.5 MAC behind the wing.

have higher loads on either side, also the curves are integrated. This actually lead to very similar values of 2.0827 for InstalledProp Loading, and 2.0804 for the IsolatedProp Loading. Overall, in this cross section it can be seen that the installed case leads to higher axial velocity and total pressure, which means that the presence of the wing for the propeller loading leads to a higher loading overall in this case.

Also the swirl loading of the two loading cases are very similar. In Figure A.5 the swirl angle for both

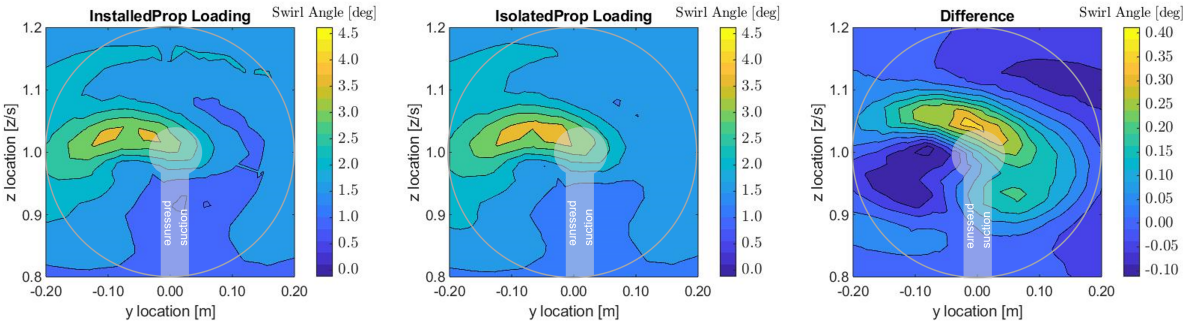

Figure A.5: Swirl angle 1.5 MAC behind the wing. Difference going from installed to isolated.

cases and the difference between these angles are plotted. Interestingly, the highest swirls are around and above the wing tip while the peak in the difference is centered below the wing tip. The isolated propeller loading case has higher swirl angles with a difference of up to 0.35 °.

The trend is the same, but the peaks are higher or lower for the installed case. It is understandable that these differences present between the two loading cases, but is not expected that the flow field characteristics change sufficiently to deem the installed loading unreliable. Therefore, the isolated propeller loading is used for the further research.

B

Pressure fluctuations

In this appendix, the pressure fluctuations found on the wing are discussed. These have come up at two instances: the span distribution of the drag has dips around 10% chord, and the wing-only configuration with and without the nacelle show higher fluctuations on the pressure side of the leading edge.

In the span distribution of the drag, the drag coefficients drop with 30% at multiple wing section cuts. This can be seen in Figure B.1a. At the location of these cuts the chord pressure distribution looks like Figure B.1b 'dip', comparing with a section next to it at 10% span ('0.1'). It can be observed that on the pressure side leading edge, a slight fluctuation occurs at the location with the dip. It is almost not distinguishable, and also not visible on pressure contour graphs.

Furthermore, a similar but bigger pressure fluctuation is observed at 90% chord when plotting the pressure along the chord. This location is chosen because the difference in lift observed in the span loading in chapter 4. The pressure distribution in Figure B.2 shows the effect of removing or adding the nacelle. First of all, it can be observed that adding the nacelle shifts the suction pressure to a higher value, thus this confirms that lift is increased locally. This would be explained by the presence of the nacelle acting as a wingtip, thus maintaining the higher pressure difference. These graphs also show an unexpected behaviour at the leading edge, in the wing-only configuration. A leading edge pressure pulsation on the pressure side of the wing is observed in Figure B.2. When investigated, this behaviour is observed throughout the span of the wing. The origin of these pressure pulsations are shown in Figure B.3, where the pressure contour on the pressure side leading edge of both the cases with and cases without the nacelle is plotted.

It is expected that this effect is caused by a modelling choices made. Previous simulation results before subsection 3.2.7 do not show this phenomenon. Thus, it is likely an effect of the mesh locally that results in the difference of showing this fluctuation or not.

So specifically the wing-only, both without the propeller ('w') and with the propeller ('wp') model shows pressure fluctuations around the leading edge pressure side. These fluctuations are visible, and biggest in the Cp-c graph, around the tip of the wing. At the root of the wing, the pressure fluctuations may lead to dips in the calculated drag coefficient at some sections.

Nevertheless, these pressure fluctuations shown are not expected to affect the rest of the results significantly. At the root, the effect is very local and the resulting error when integrating the drag is small. Although this effect seems local and not affecting integrated values, it does imply a limitation in research on the local pressure distributions. On the other hand, the overall trends in the span distributions are comparable to each other. So it can be justified that relative conclusions in this research can still be drawn.

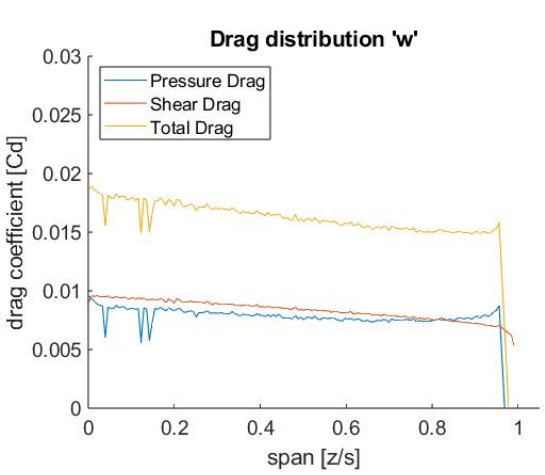

(a) Drag distribution, showing dip in pressure drag near (z/s = 0.1)

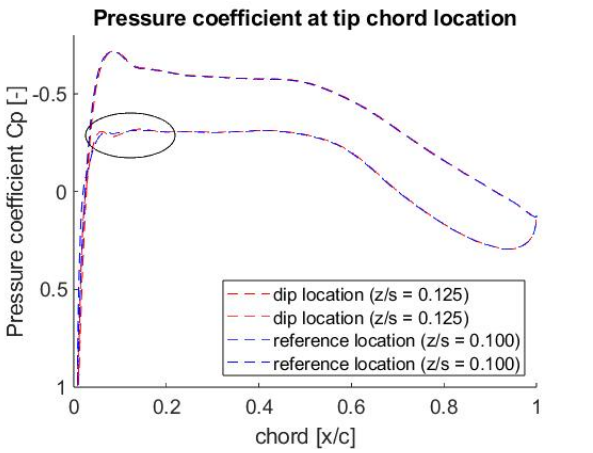

(b) Chord pressure distribution, showing pressure fluctuation in red near leading edge.

Figure B.1: Dips in drag distribution near root and corresponding pressure-chord graph.

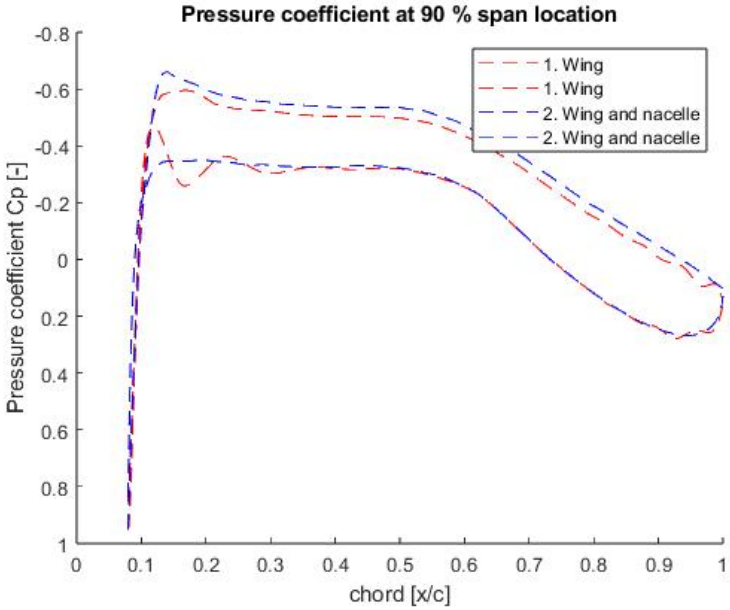

Figure B.2: Pressure coefficient chord distribution at 90% span.

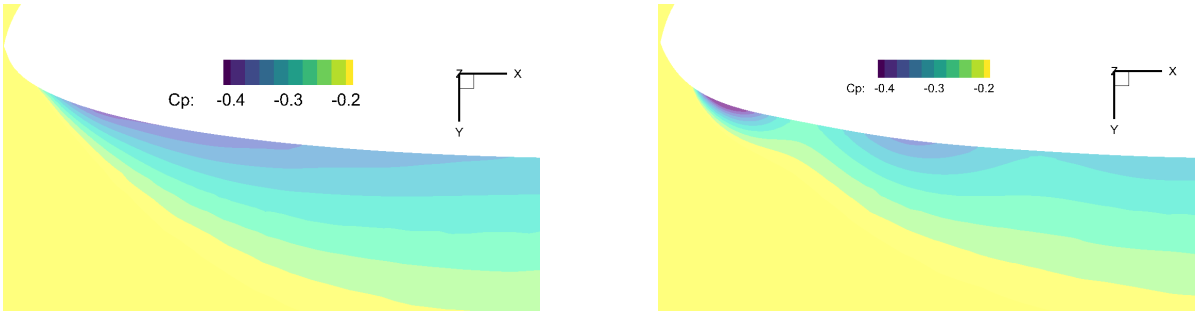

(a) Nacelle is present.

(b) No nacelle is present

Figure B.3: Pressure coefficient at pressure side leading edge at 90% span.